



**KTH Chemical Science  
and Engineering**

# Hydrophobic surfaces: Effect of surface structure on wetting and interaction forces

PETRA HANSSON



Doctoral Thesis at the Royal Institute of Technology  
Stockholm 2012

Akademisk avhandling som med tillstånd av Kungliga Tekniska Högskolan  
framläggs till offentlig granskning för avläggande av teknologie  
doktorsexamen fredagen den 2 november 2012 kl 10.00 i sal F3, KTH,  
Lindstedtsvägen 26, Stockholm.

**Petra Hansson.** *Hydrophobic surfaces: Effect of surface  
structure on wetting and interaction forces*

TRITA-CHE Report 2012:52  
ISSN 1654-1081  
ISBN 978-91-7501-506-4  
YKI Publication A-3055

Denna avhandling är skyddad enligt upphovsrättslagen. Alla rättigheter  
förbehålles.

Copyright © 2012 Petra Hansson. All rights reserved. No part of this thesis  
may be reproduced without permission from the author.

The following papers are printed with permission:  
Paper I: Copyright © Royal Society of Chemistry  
Paper II, III and V: Copyright © American Chemical Society

Printed at E-Print, Stockholm 2012

# Abstract

The use of hydrophobic and superhydrophobic surfaces is of importance for many processes both in nature and industry. Interactions between hydrophobic species and their wetting behavior play a key role in industrial applications such as water-cleaning procedures, pitch control during papermaking, flotation processes but they also give information on how to design surfaces like hydrophobic mineral pigments.

In this thesis, the influence of surface structure, roughness and chemistry on wetting and surface interaction forces has been studied. This was achieved by preparing surfaces with a defined structure and roughness. Surfaces with hexagonally close-packed particles, pore arrays, randomly deposited nanoparticles as well as flat reference surfaces were prepared. The atomic force microscope (AFM) was utilized for surface characterization as well as force and friction measurements while contact angles and confocal Raman microscopy experiments were mainly used for wetting studies.

The deposition of silica particles in the size range of nano- to micrometers using the Langmuir-Blodgett (LB) technique resulted in ordered particle coated surfaces exhibiting hexagonal close-packing and close to Wenzel state wetting after hydrophobization. Force measurements using these particle coated surfaces displayed long-range interaction forces assigned to be a consequence of air cavitation between the surfaces. Smaller roughness features provided larger forces and interaction distances interpreted as being due to fewer restrictions of capillary growth. Friction measurements proved both the surface structure and chemistry to be important for the observed frictional forces.

Wetting on hydrophobic pore array surfaces were shown not to be described by the well-established Wenzel or Cassie-Baxter models. Instead, the three-phase contact line of water droplets avoided the pores which created a jagged interface. The influence of the pores was evident in force curves measured in water, both in terms of the shape, in which the three-phase contact line movements around the pores could be detected, as well as the depth of the pores providing different access and amount of air. When

water/ethanol mixtures were used, the interactions, displaying no sign of air cavities, were concluded to be due to ethanol condensation.

Confocal Raman microscopy experiments with water and water/ethanol mixtures on superhydrophobic surfaces gave evidence for water depletion and ethanol/air accumulation close to the surface. Force measurements using superhydrophobic surfaces showed extremely long-range interaction distances of several micrometers.

This work has provided evidence for air cavitation between hydrophobic surfaces in aqueous solution. It was also shown that the range and magnitude of interaction forces could, to some extent, be predicted by looking at certain surface features like structure, roughness and the overall length scales.

**Key words:** hydrophobic surface, superhydrophobic surface, atomic force microscopy, surface forces, capillary forces, cavitation, surface roughness, friction, wetting, confocal Raman, contact angles, surface preparation, Langmuir-Blodgett

# Sammanfattning

Hydrofoba och superhydrofoba ytor samt dess egenskaper är viktiga för en lång rad industriella processer såsom vattenrening, hartskontroll vid papperstillverkning, flotation och många fler men också för att skraddarsy, till exempel, hydrofoba ytor av mineralpigment. Denna avhandling behandlar hur egenskaper hos en yta, till exempel strukturen, ytråheten och kemin, påverkar krafter mellan och vätning på hydrofoba ytor. Ytor med tätpackade partiklar, ordnade porer, godtyckligt deponerade nanopartiklar samt plana referensytor tillverkades och studerades. Ett atomkraftsmikroskop (AFM) användes för att karaktärisera ytor samt mäta krafter och friktion medan vätning studerades genom mätningar av kontaktvinklar och konfokal Ramanmikroskopi.

Genom att deponera silikapartiklar i storleksordningen nano- till mikrometer med användning av Langmuir-Blodgettekniken (LB) kunde ytor med hexagonalt ordnade partiklar och vätning i Wenzelregimen produceras. Kraftmätningar med dessa partikelytor i vatten visade på väldigt långväga krafter som antas uppkomma genom att luft bildar kaviteter mellan ytorna. Lägre grad av ytråhet gav upphov till starkare krafter och mer långväga interaktioner, vilket tolkades som en konsekvens av minskad begränsning för kapillären att växa. Friktionsmätningar visade att både ytstrukturen och kemin påverkar de uppmätta friktionskrafterna.

Vättningsstudier gjorda på hydrofoba porösa ytor visade att varken Wenzel- eller Cassie-Baxtermodellen kunde tillämpas. Studier av kraftkurvor från mätningar i vatten visade tydligt att porerna påverkar både formen på kurvan samt att pordjupet bestämde avstånden på växelverkan genom att ge tillgång till luft på olika djup och i olika mängd. Växelverkan uppmätt i vatten/etanolblandningar verkade uppstå på grund av kondensering av etanol snarare än luftkaviteter.

Konfokal Ramanmikroskopi användes för att studera superhydrofoba ytor täckta med vatten och vatten/etanol, vilket gav bevis för att vatten trängs bort från ytan medan etanol och/eller luft ackumuleras. Kraftmätningar med

superhydrofoba ytor gav upphov till extremt långväga interaktioner på flera mikrometer.

Den här avhandlingen har påvisat förekomsten av luftkaviteter nära hydrofoba ytor i vattenlösning. Storleken och avståndet på krafter mellan ytorna har även visat sig kunna, till stor del, förutspås genom att undersöka ytstrukturen och ytråheten.

# List of Papers

This thesis is based on the following papers, which are referred to in the text by their Roman numerals.

- I     **Solvent segregation and capillary evaporation at a superhydrophobic surface investigated by confocal Raman microscopy and force measurements**  
Brandner, B. D., Hansson, P. M., Swerin, A., Claesson, P. M., Wåhländer, M., Schoelkopf, J., Gane, P. A. C.  
*Soft Matter*, **2011**, 7, 1045-1052.
  
- II    **Robust hydrophobic surfaces displaying different surface roughness scales while maintaining the same wettability**  
Hansson, P. M., Skedung, L., Claesson, P. M., Swerin, A., Schoelkopf, J., Gane, P. A. C., Rutland, M. W., Thormann, E.  
*Langmuir*, **2011**, 27, 8153-8159.
  
- III   **Influence of surface topography on the interactions between nanostructured hydrophobic surfaces**  
Hansson, P. M., Swerin, A., Schoelkopf, J., Gane, P. A. C., Thormann, E.  
*Langmuir*, **2012**, 28, 8026-8034.
  
- IV    **Frictional forces between hydrophilic and hydrophobic particle coated nanostructured surfaces**  
Hansson, P. M., Claesson, P. M., Swerin, A., Schoelkopf, J., Gane, P. A. C., Thormann, E.  
*manuscript*
  
- V     **Effect of surface depressions on wetting and interactions between hydrophobic pore array surfaces**  
Hansson, P. M., Hormozan, Y., Brandner, B. D., Linnros, J., Claesson, P. M., Swerin, A., Schoelkopf, J., Gane, P. A. C., Thormann, E.  
*Langmuir*, **2012**, 28, 11121-11130.
  
- VI    **Hydrophobic pore array surfaces: Wetting and interaction forces in water/ethanol mixtures**  
Hansson, P. M., Hormozan, Y., Brandner, B. D., Linnros, J., Claesson, P. M., Swerin, A., Schoelkopf, J., Gane, P. A. C., Thormann, E.  
*submitted for publication*

The author's contribution to the papers was as follows:

- I        Part of experimental work, part of manuscript preparation
- II       Major part of experimental work, part of manuscript preparation
- III-IV   All experimental work, major part of manuscript preparation
- V-VI   Major part of experimental work, major part of manuscript preparation



# Table of contents

Abstract .....	iii
Sammanfattning .....	v
List of Papers .....	vii
Abbreviations and Symbols .....	xi
1 Introduction .....	1
1.1 Hydrophobicity and superhydrophobicity .....	1
1.2 Hydrophobicity in nature .....	2
1.3 Applications related to hydrophobicity .....	3
2 Theory .....	5
2.1 Surface structure .....	5
2.2 Surface forces .....	6
2.2.1 DLVO theory .....	7
2.2.2 Interaction forces between hydrophobic surfaces .....	11
2.2.3 Adhesion .....	15
2.3 Friction .....	16
2.4 Wetting .....	17
2.4.1 Wenzel state .....	18
2.4.2 Cassie-Baxter state .....	19
2.4.3 Transitions between Wenzel and Cassie – Intermediate situations .....	19
2.4.4 Validity of the assumptions underlying the Wenzel and Cassie-Baxter models .....	19
3 Experimental .....	21
3.1 Atomic force microscopy .....	21
3.1.1 Imaging .....	22
3.1.2 Force .....	23
3.1.3 Friction .....	24
3.1.4 Contact angle of colloidal probe .....	25
3.2 Confocal Raman microscopy .....	26
3.3 Contact angles .....	28
3.4 Surface preparation .....	28

3.4.1 Langmuir-Blodgett .....	28
3.4.2 Lithography and etching .....	29
3.4.3 Dip coating .....	30
3.4.4 Sintering .....	30
3.4.5 Silanization .....	31
4 Results .....	32
4.1 Surface preparation .....	32
4.1.1 Particle coated surfaces – Langmuir-Blodgett deposition .....	32
4.1.2 Pore array surfaces – Photolithography and etching .....	34
4.1.3 Superhydrophobic surfaces – Dip coating .....	35
4.2 Surface characterization .....	36
4.2.1 Particle coated surfaces – Hexagonal structure and robustness ....	36
4.2.2 Pore array surfaces – Structure of three-phase contact line and water penetration into the pores .....	38
4.2.3 Superhydrophobic surface – Lotus effect .....	41
4.3 Force measurements .....	41
4.3.1 Particle coated surfaces – Dependence on roughness length scale and extremely long-range forces .....	42
4.3.2 Pore array surfaces – Consequences of pores observed in the force curves .....	45
4.3.3 Superhydrophobic surfaces – Long-range forces .....	48
4.4 Friction measurements .....	49
4.4.1 Particle coated surfaces – Amontonian or adhesion controlled friction .....	50
4.5 Capillary effects .....	51
4.5.1 Detection of air/water vapor and accumulation of ethanol on superhydrophobic surfaces .....	52
4.5.2 Influence of ethanol – removal of capillary forces .....	53
4.6 General discussions about interactions between hydrophobic surfaces.	55
5 Conclusions .....	59
6 Future work .....	62
7 Acknowledgements .....	64
8 References .....	66

# Abbreviations and Symbols

## Abbreviations:

AFM	Atomic force microscopy
DLS	Dynamic light scattering
DLVO	Derjaguin-Landau-Verwey-Overbeek
DNA	Deoxyribonucleic acid
EDL	Electrostatic double layer
FWHM	Full width half maximum
HRSEM	High resolution scanning electron microscopy
IR	Infra-red
JKR	Johnson-Kendall-Roberts
LB	Langmuir-Blodgett
NA	Numerical aperture
$\pi$ -A	Surface pressure-area
PB	Poisson-Boltzmann
SEM	Scanning electron microscopy
SFA	Surface force apparatus
vdW	van der Waals
VSFS	Vibrational sum frequency spectroscopy

## Symbols:

$A$	Hamaker constant (J)
$\alpha$	polarizability ( $\text{C m}^2 \text{ V}^{-1}$ )
$\alpha_0$	normal detector sensitivity ( $\text{m V}^{-1}$ )
$c$	molar concentration ( $\text{mol dm}^{-3}$ )
$c_m$	concentration per $\text{m}^3$
$D$	distance, surface separation (m)
$\Delta$	relative change
$\delta$	torsional detector sensitivity ( $\text{V rad}^{-1}$ )
$\varepsilon$	relative permittivity
$\varepsilon_0$	permittivity of free space ( $8.854 \times 10^{-12} \text{ C}^2 \text{ J}^{-1} \text{ m}^{-1}$ )
$F$	force (N)
$f$	area fraction
$F_{\text{adh}}$	adhesion force (N)
$F_{\text{cap}}$	capillary force (N)
$F_f$	frictional force (N)
$F_N$	normal force (N)

$F_{\text{vdW}}$	van der Waals force (N)
$\gamma$	surface tension ( $\text{N m}^{-1}$ )
$\gamma_{\text{int}}$	interfacial tension ( $\text{N m}^{-1}$ )
$h$	Planck's constant ( $6.626 \times 10^{-34} \text{ J s}$ )
$h_{\text{eff}}$	effective height (m)
$\eta$	viscosity ( $\text{Pa s}$ )
$k_{\text{B}}$	Boltzmann's constant ( $1.381 \times 10^{-23} \text{ J K}^{-1}$ )
$k_{\text{n}}$	normal spring constant ( $\text{N m}^{-1}$ )
$k_{\text{t}}$	torsional spring constant ( $\text{Nm rad}^{-1}$ )
$\kappa^{-1}$	Debye length (m)
$\lambda$	wavelength (m)
$\mu$	coefficient of friction
$\mu_{\text{i}}$	dipole moment (C m)
$N$	number of points
$n$	refractive index
$\nu$	ionization frequency (Hz)
$\nu_{\text{e}}$	main electronic absorption frequency (Hz)
$P$	pressure (Pa)
$P_0$	saturation vapor pressure (Pa)
$R$	radius (m) or molar gas constant ( $8.314 \text{ J K}^{-1} \text{ mol}^{-1}$ )
$R_{\text{a}}$	arithmetic mean roughness (m)
$R_{\text{N}}$	normalized radius (m)
$R_{\text{q}}$	root mean square roughness (m)
$r$	curvature ( $\text{m}^{-1}$ ) or roughness factor
$\rho$	density ( $\text{kg m}^{-3}$ )
$T$	temperature ( $^{\circ}\text{C}$ or K)
$\theta$	contact angle ( $^{\circ}$ )
$\beta$	angle against normal plane ( $^{\circ}$ )
$V_{\text{cap}}$	capillary volume ( $\text{m}^3$ )
$V_{\text{f}}$	lateral photodetector signal (V)
$V_{\text{m}}$	molar volume ( $\text{m}^3 \text{ mol}^{-1}$ )
$W$	interaction free energy (J)
$W_{\text{adh}}$	work of adhesion (J)
$Z_{\text{ave}}$	average value, value at central plane
$Z_{\text{i}}$	local value
$z$	ion valency

# 1 Introduction

The aim of this thesis work was to investigate how surface structures influence wetting and interaction forces between hydrophobic surfaces. In order to understand this rather complex phenomenon, a background to the meaning of hydrophobicity/superhydrophobicity and an explanation of the importance of the hydrophobic properties through its use in nature and in technical applications are provided in this chapter.

## 1.1 Hydrophobicity and superhydrophobicity

The concepts of hydrophobicity (*Greek*: hydro = water and phobos = fear) and superhydrophobicity are of vital importance both for fundamental purposes as well as in industrial applications. Interest in this type of surface property has grown substantially during the past years due to understanding of the criteria for forming superhydrophobic surfaces and recognition of its potential as, for example, liquid barriers in different applications. The simplest explanation of hydrophobicity is a surface having a static water contact angle higher than  $90^\circ$ , while a superhydrophobic surface is supposed to exhibit a contact angle higher than  $150^\circ$ , as shown in Figure 1-1. The high contact angle is often accompanied by a small roll-off angle, *i.e.* the liquid easily bounces or rolls off the surface.

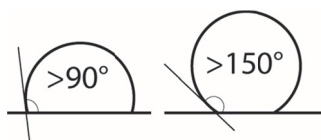


**Figure 1-1.** Schematic illustration showing a macroscopic water droplet on a hydrophobic surface with a contact angle higher than  $90^\circ$  and a superhydrophobic surface displaying a contact angle above  $150^\circ$ .

## 1.2 Hydrophobicity in nature

There exist numerous examples of species exhibiting superhydrophobicity in nature (Figure 1-2), among which the lotus flower (*Nelumbo nucifera*) must be the most well-known. The self-cleaning property, “the lotus effect”, displayed by some superhydrophobic surfaces is even named after the plant. The high contact angles and the low roll-off angles were noticed a long time ago but the underlying mechanism was not realized until the end of the 20<sup>th</sup> century, when Barthlott and Neinhuis systematically recorded images of the micro- and nanostructures of the leaf.<sup>1,2</sup> They found that hierarchical structures, *i.e.* combination of roughness in both the micro- and nanometer scale, together with a low surface energy wax layer were the origin of the superhydrophobicity. The self-cleaning effect of the lotus implies an extremely low roll-off angle of water droplets which means a small hysteresis between advancing and receding contact angles. This is in contrast to some other plants exhibiting the so-called petal effect, where the rose (*Rosa rubiginosa*) is the most studied, that have a high contact angle but also a high adhesion, *i.e.* a high roll-off angle, between the surface and a water droplet. This is due to penetration of the droplet into the nanostructured layer but not the microstructures underneath.<sup>3,4</sup>



**Figure 1-2.** Two photographs showing hydrophobic surfaces in nature. In the left figure, water easily rolls off the surface of the lady's cape leaf while the figure to the right displays a rose plant with very high adhesion between the droplet and the surface.

In addition to many leaves of plants, several insects also have the ability to resist water spreading on their wing surfaces. The water strider (*Gerris remigis*) with its non-wetting legs that enable the insect to stand on a water surface is one of the most well-known examples.<sup>5</sup> Other insects showing superhydrophobic properties are butterflies and cicadas which give them the possibility to stay dry and clean.<sup>6</sup> Also, many birds have feathers with the capability to resist spreading of water during swimming.

Another important phenomenon governed by interactions between hydrophobic materials is the folding of proteins, the biomacromolecules consisting of a chain of amino acids and encoded for by deoxyribonucleic acid (DNA). Protein misfolding can originate from disturbances in the hydrophobicity/hydrophilicity of the interacting molecules and is known to cause severe neurological diseases such as Alzheimer's, Parkinson's and Creutzfeldt-Jakob disease.<sup>7,8</sup>

### 1.3 Applications related to hydrophobicity

The fundamental studies on how to prepare superhydrophobic surfaces and how their properties can be explained have increased enormously during the last decade. Today, superhydrophobic surfaces should not only display water repellency but also exhibit, for example, transparency, specific colors and flexibility.<sup>9</sup> As the number of fundamental studies increases, more and more industrial applications on hydrophobic or superhydrophobic materials are realized. Its use as corrosion protection,<sup>10,11</sup> in de- or antiicing applications,<sup>12,13</sup> as coatings in liquid resistant papers<sup>14,15</sup> or in fabrics,<sup>16,17</sup> has been a recent focus of interest and the number of applications will most likely continue to rise.

An increased understanding of the influence of hydrophobic materials on surface interactions is of importance for many industries. In deinking, the forces between the cellulose fibers and the ink particles are a key issue during separation.<sup>18</sup> Flotation processes, such as froth flotation in the mining industry as well as waste water treatment, demand a high degree of knowledge about hydrophobic materials.<sup>19</sup> Control of sticky materials,

pitch, in wood is of vital importance in pulp and paper making processes due to the stickiness causing severe problems and cost for the industry.<sup>20</sup> In summary, more detailed knowledge about the interactions between different hydrophobic species is a prerequisite for development of materials and processes in many different types of industries.



## 2 Theory

This chapter presents the theoretical background for the most important phenomena needed in order to be able to interpret and understand the obtained results. Definitions of surface structure and presentations of relevant surface forces and wetting theories are discussed. Also, previous work in the field is introduced.

### 2.1 Surface structure

The structure of a surface is an important property and, together with for example the material and the size, it is deciding its overall quality. Surface structure is often characterized in terms of the surface roughness. The most common ways to measure surface roughness are, if the roughness length scales are in the micrometer range, by profilometry while atomic force microscopy (AFM) often is used for surfaces with length scales in the nanometer range. Several different parameters can be extracted from a roughness measurement but two of the most commonly discussed are the root mean square roughness,  $R_q$ , and the arithmetic mean roughness value,  $R_a$ , as given by:

$$R_q = \sqrt{\frac{\sum_{i=1}^N (Z_i - Z_{ave})^2}{N}} \quad (2-1)$$

where  $Z_{ave}$  = average  $Z$  value within the given area,  $Z_i$  = local  $Z$  value and  $N$  = number of points within the given area and

$$R_a = \frac{\sum_{i=1}^N |Z_i - Z_{ave}|}{N} \quad (2-2)$$

where  $Z_{ave}$  =  $Z$  value at the central plane,  $Z_i$  = local  $Z$  value and  $N$  = number of points within the given area. The roughness parameters

mentioned above only describe the height variance in lateral direction and do not give any information about the actual shape of the surface structures. When fabricating superhydrophobic surfaces it has been noted that many different structures can give rise to surfaces with a high contact angle as long as they introduce a certain roughness together with a low surface energy. Surfaces consisting of multilayers of particles and/or polymers,<sup>21</sup> deposited particles,<sup>22,23</sup> etched or deposited pillars<sup>24,25</sup> or pores<sup>26</sup> are all examples of some of the possible structures that can be used to produce a superhydrophobic surface.

## 2.2 Surface forces

The concept of surface and intermolecular forces is of fundamental importance to the issues discussed in this thesis. Intermolecular forces are always present and they always affect molecules in solution, in solid materials and at interfaces. The collective effect of intermolecular forces between two larger bodies (particles/surfaces) is known as surface forces and they are subdivided into different classes depending on the molecular origin. Electrostatic forces, van der Waals forces and interactions between hydrophobic surfaces and its possible origins are most relevant for this work and they will be presented briefly below and can be seen in Figure 2-1.

In order to accurately measure quantitative forces between surfaces, the geometry of the surfaces needs to be taken into consideration. This is done through the Derjaguin approximation which relates the measured force,  $F$ , to the interaction free energy per unit area,  $W$ , for two flat surfaces separated by a distance,  $D$ , according to:<sup>27</sup>

$$W(D) = \frac{F(D)}{2\pi R_N} \quad (2-3).$$

$R_N$  is the normalized radius that depends on the geometry of the interacting objects, *e.g.* a sphere-flat geometry gives  $R_N = R_{\text{sphere}}$  and crossed cylinders give  $R_N = \sqrt{R_{\text{cylinder1}} R_{\text{cylinder2}}}$ . The Derjaguin

approximation is valid when  $R \gg D$ , the surfaces are non-deformable and  $\partial W/\partial D$  is continuous.

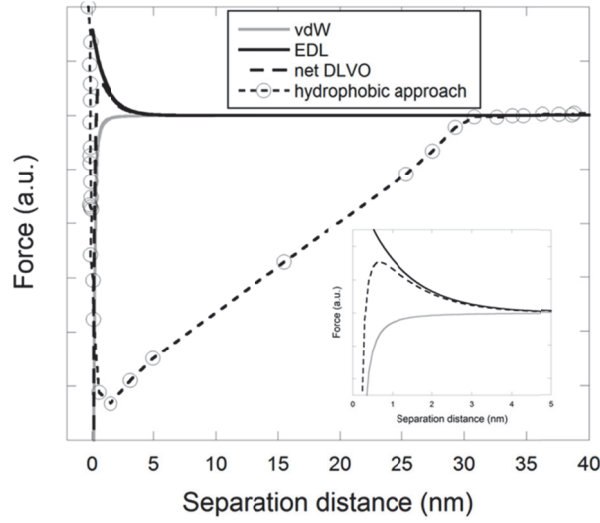


**Figure 2-1.** Summary of the most relevant forces in this thesis; the DLVO force and the van der Waals and electrostatic double layer forces contributing to DLVO together with a typical approach curve for a measurement between two hydrophobic surfaces in aqueous solution.

### 2.2.1 DLVO theory

The theory on the stability of colloidal particles, *i.e.* the combination of electrostatic double layer forces and van der Waals forces, is generally referred to as the Derjaguin-Landau-Verwey-Overbeek (DLVO)<sup>28,29</sup> forces and the DLVO interaction free energy is simply calculated from the sum of the contributions from the electrostatic double layer,  $W_{\text{edl}}(D)$ , and van der Waals,  $W_{\text{vdW}}(D)$ , interactions by

$$W(D) = W_{\text{edl}}(D) + W_{\text{vdW}}(D) \quad (2-4).$$

#### 2.2.1.1 van der Waals interactions

The van der Waals force is a collective name describing the orientation (Keesom), induction (Debye) and dispersion (London) forces arising from displacement of permanent or induced dipoles in the molecules and

they always have to be considered when discussing forces between molecules. Two molecules with permanent dipoles and the ability to rotate nearly freely will preferentially align themselves along their opposite charges and therefore attract each other. The corresponding dipole-dipole interaction energy is referred to as the Keesom energy:<sup>30</sup>

$$W(D) = -\frac{\mu_1^2 \mu_2^2}{3(4\pi\epsilon_0\epsilon)^2 k_B T D^6} \quad (2-5)$$

where  $\mu_i$  is the dipole moment for molecule  $i$ . Eq. 2-5 is valid for nearly freely rotating dipoles which means  $k_B T > \mu_1^2 \mu_2^2 / 4\pi\epsilon_0\epsilon D^3$ , and thus energetically favorable orientations between the dipoles are slightly preferred.

A polar molecule in close proximity to another molecule will induce a dipole which results in an attractive force as described as follows according to Debye:<sup>31</sup>

$$W(D) = -\frac{\mu^2 \alpha}{(4\pi\epsilon_0)^2 D^6} \quad (2-6)$$

where  $\alpha$  is the the polarizability of the neutral molecule.

The third and last contribution to the van der Waals force is the London forces. In contrast to the Keesom and Debye forces, these dispersive forces cannot be calculated using classical physics but quantum mechanical perturbation theory must be involved. All atoms have, at every moment, a dipole moment due to displacement of their electron clouds. If several atoms are bonded together to form a molecule, this effect is even more pronounced and the created instantaneous dipole has the ability to affect other molecules in the surrounding. These induced dipoles can attract or repel each other. Two molecules with ionization frequencies of  $\nu_1$  and  $\nu_2$  have a total free energy from the London forces described by:<sup>32</sup>

$$W(D) = -\frac{3}{2} \frac{\alpha_1 \alpha_2}{(4\pi\epsilon_0)^2 D^6} \frac{h\nu_1 \nu_2}{(\nu_1 + \nu_2)} \quad (2-7).$$

Eqs. 2-5 to 2-7 are applicable to a pair of molecules interacting across vacuum. When van der Waals forces between macroscopic bodies are considered, many body effects and the fact that a medium is present between the bodies will affect the van der Waals interaction and therefore need to be considered.

The van der Waals force between macroscopic bodies is calculated using the Hamaker constant,  $A$ . It was first derived by incorrectly assuming pairwise additivity of the forces from all the molecules in the macroscopic surface.<sup>33-35</sup> Lifshitz later made a more rigorous, but also more complex, calculation and found an expression for the Hamaker constant based on the bulk dielectric properties of the material according to:

$$A = \frac{3}{4} k_B T \left( \frac{\varepsilon_1 - \varepsilon_3}{\varepsilon_1 + \varepsilon_3} \right)^2 + \frac{3\nu_e}{16\sqrt{2}} \frac{(n_1^2 - n_3^2)^2}{(n_1^2 + n_3^2)^{3/2}} \quad (2-8)$$

where  $\varepsilon_i$  is the static dielectric constant for medium  $i$ ,  $\nu_e$  is the main electronic absorption frequency in the UV region and  $n_i$  is the refractive index of medium  $i$  in the visible region.<sup>36</sup> Eq. 2-8 is valid for two identical materials (1) interacting through another medium (3). In most cases, the macroscopic van der Waals force is attractive but a repulsive force is also possible for certain material combinations.<sup>37,38</sup>

For the geometry used in this thesis, that is a flat surface interacting with a spherical particle, the van der Waals force can be calculated using

$$\frac{F_{vdW}}{R} = - \frac{A}{6D^2} \quad (2-9).$$

For other geometries similar expressions can be derived.<sup>39</sup>

### 2.2.1.2 Electrostatic double layer interactions

Most of the experiments included in this thesis have been performed in water or in water mixtures. Due to its very high dielectric constant, water is a good solvent for ions. The dissociation of surface groups and adsorption of charged molecules make almost all surfaces in water

charged. The electric field created by the charged surface gives enrichment in the concentration of counterions, *i.e.* the ion with opposite charge and depletion of co-ions, *i.e.* the ions with the same charge as the surface, in close proximity to the surface. This layer of surface charges and ions is referred to as the “electrostatic double layer”. The decay of surface potential with respect to distance from the surface is described by the Debye length,  $\kappa^{-1}$ , which can be calculated using:

$$\kappa^{-1} = \left( \frac{\epsilon \epsilon_0 k_B T}{e^2 \sum_i c_{mi} z_i^2} \right)^{1/2} \quad (2-10)$$

where  $z_i$  is the valency of the ions and  $c_m$  is the concentration of the electrolyte per  $m^3$ . For an aqueous NaCl solutions, the equation can be simplified to read

$$\kappa^{-1} = \frac{0.304}{\sqrt{c}} \quad (2-11)$$

where  $c$  is the molar concentration of the ions.

When two surfaces in water are approaching each other, their electrostatic double layers will, at some point, overlap and induce a repulsive force approximately described by an exponentially decaying equation:

$$W(D)_{\text{edl}} = C e^{-\kappa D} \quad (2-12)$$

where  $C$  is a constant that depends on the surface geometries, their surface charge density and the solution. It is determined by solving the Poisson-Boltzmann (PB) equation for the particular system.<sup>40,41</sup> A numerical solution of the PB equation must be used for small surface separations to extract the exact double layer force. In the force studies presented in this work, a 10 mM NaCl aqueous solution has in most cases been used as the liquid medium in order to partly screen the electrostatic interactions and to calculate the contribution of the double layer force in relation to the measured forces.

## 2.2.2 Interaction forces between hydrophobic surfaces

Just as phase separation of water and oil occurs due to unfavorable conditions of enthalpy exceeding that of entropy, hydrophobic species in water attract each other, thus lowering the total free energy of the system by minimizing the area exposed to water. The first measurement of interactions between hydrophobic surfaces in aqueous solution was performed by Israelachvili and Pashley in 1982 using the surface force apparatus (SFA).<sup>42</sup> Their study was soon followed by others who investigated and tried to interpret the extremely long-range interactions of sometimes several hundreds of nanometers, much longer than the expected van der Waals force, as can be seen in Figure 2-1.<sup>43-46</sup> The sharp jump-in at a distance of several tens of nanometers as well as a retract curve showing an exponential decay are the well-known features for such a force curve. There is still an on-going debate regarding the mechanism behind the origin of the interactions and several suggestions have been proposed. Here follow short descriptions of some of the most frequently used explanations for this “hydrophobic interaction”:

### 2.2.2.1 Cavitation/bridging bubbles

Cavitation or bridging bubbles due to dissolved gas in water soon became the most plausible explanation for the observed interactions between hydrophobic surfaces<sup>45,47,48</sup> and the mechanism has continued to be used to explain many of the results obtained.<sup>20,49-56</sup> Figure 2-2 shows the proposed mechanism for cavity formation between hydrophobic surfaces. This theory is somewhat supported by the observation that by degassing the water, the range and magnitude of the interaction decrease even though it does not disappear completely.<sup>57,58</sup> However, most liquid cells used during force measurements are open to the surroundings which mean that water is saturated with air shortly after degassing.

The proposed air bridges can either be formed from a thin air/water vapor layer or from micrometer or nanometer sized air bubbles resting on the surface. Even though the Laplace pressure states that the pressure inside the nanobubbles should be too high for them to be stable, numerous studies have shown both their existence as well as their apparent stability for hours.<sup>51,59-63</sup> In order to study the nanobubbles in detail, a protocol for

nanobubble formation is often used. This was developed by Zhang *et al.* who utilized that gases have different solubility in different solvents, *e.g.* water and ethanol. Thus, by changing the solvent during a measurement, nanobubbles can be formed in a controlled manner.<sup>58,64</sup> Imaging of nanobubbles shows, in some cases, spherically shaped isolated bubbles<sup>65,66</sup> while other studies indicate more irregular bubbles distributed like a continuous film.<sup>67,68</sup> Also, more indirect methods have been used to image air close to a hydrophobic surface providing evidence of cavitation being the main source behind the long-range forces.<sup>69,70</sup> The similarity of the resulting force curves measured between hydrophobic surfaces in water and hydrophilic surfaces in a humid atmosphere indicates that both are due to capillary condensation/evaporation.<sup>71</sup> The theory of capillary forces is of importance for this thesis and has therefore been assigned a section of its own.



**Figure 2-2.** Schematic illustration of cavitation between two hydrophobic surfaces in aqueous solution. In a) the surfaces are completely separated and there are no interactions between them and in b) an air cavity between them is formed on approach and they jump together. c) The surfaces are in direct contact before they d) are separated which is accompanied by extension of the air cavity until it e) breaks

#### 2.2.2.1.1 Capillary forces

Conventionally, capillary forces are thought to occur by formation of a liquid meniscus around the contact areas of particles or macroscopic surfaces in a humid environment. However, they can also appear in the form of a liquid bridge in another immiscible liquid or as gas bridges in a liquid. Capillary condensation is the result of the two interacting surfaces being lyophilic with respect to the vapor in the surrounding environment. This will make the vapor condense between the surfaces as described by the Kelvin equation:<sup>72</sup>

$$RT \ln \frac{P}{P_0} = \gamma V_m \left( \frac{1}{r_1} + \frac{1}{r_2} \right) \quad (2-13).$$



$r_1$  and  $r_2$  describe the curvature of the meniscus,  $P$  is the actual vapor pressure,  $P_0$  is the saturation vapor pressure,  $\gamma$  is the surface tension and  $V_m$  is the molar volume of the condensing liquid.

The capillary force,  $F_{\text{cap}}$ , between a sphere, with radius  $R$ , and a surface can be calculated using the following expression:<sup>73</sup>

$$F_{\text{cap}} = 4\pi\gamma s R \left(1 - \frac{D}{\sqrt{\frac{V_{\text{cap}}}{\pi R} + D^2}}\right) \quad (2-14)$$

where

$$s = \frac{\cos(\theta_1 + \beta) + \cos\theta_2}{2} \quad (2-15).$$

Figure 2-3 shows a schematic figure of the cavity between a surface and a probe.  $D$  is the distance between the probe and the surface,  $V_{\text{cap}}$  is the volume of the capillary,  $\theta_1$  and  $\theta_2$  are the contact angles of the capillary against the surface and the probe respectively and  $\beta$  is the angle between the line starting from the center of the spherical probe going in the normal direction and towards the contact point of the capillary at the probe. Eq. 2-14 is only valid for situations with constant volume of the capillary. By introducing  $D=0$  in Eq. 2-14, the theoretical adhesion force can be calculated. When surface roughness is introduced, the situation is in general more complex with possible pinning of the three-phase contact line during cavity growth. This would give a lower adhesion force since the cavity is not allowed to grow to its optimum size.

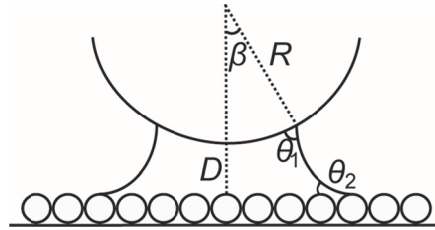


**Figure 2-3.** Illustration of the parameters included in Eq. 2-14 showing cavitation between two hydrophobic surfaces in water.

#### **2.2.2.2 Water structural effects**

Even though this thesis promotes the idea of the long-range interactions between hydrophobic surfaces being due to cavitation and capillary forces, there are other suggested mechanisms that should not be disregarded. One is restructuring of water, in which the force is said to originate from an overlap of two boundary layers of perturbed water structure when the surfaces are approaching, *i.e.* creating a surface-induced water structure.<sup>46,74</sup> This theory has mostly been used to explain interactions of a shorter-range type and fails to predict the long-range interaction forces. Another model is the so-called water bridging-cluster model, that, based on thermodynamics, assigns the interaction to depend on organized elongated water clusters between the hydrophobic surfaces.<sup>75</sup>

#### **2.2.2.3 Hydrodynamic force**

The hydrodynamic force as caused by expulsion of water from the volume between the surfaces during approach has also been suggested as a possible mechanism behind the interactions.<sup>76,77</sup> However, this is opposed by studies showing that the range and magnitude of the interactions are not affected by the approach or retract speed of the interacting surfaces.<sup>54,68</sup>

#### **2.2.2.4 Contaminations from hydrophobic species**

When using adsorbed surfactants, silanes, thiols or other types of molecules to make a surface hydrophobic, it has been suggested that these molecules can dissolve and affect the measured interactions.<sup>78</sup> This theory is contradicted by studies in which also inert surfaces are shown to give rise to the long-range interactions.<sup>79</sup> In conclusion, the subject of contamination is definitely an issue and thorough cleaning of the surfaces and other materials/equipment involved is a prerequisite to avoid uncertainties.

#### **2.2.2.5 Surface structure influence on forces between hydrophobic surfaces**

For smooth hydrophobic surfaces, the attractive forces have been found to increase with an increase in hydrophobicity as measured by the water

contact angle.<sup>80,81</sup> When the interacting surfaces instead exhibit an intrinsic roughness, the resulting forces are no longer that easy to predict. Serro and Saramago found an increased adhesion force when changing from a smooth surface to a surface with a four times higher average roughness and attributed this to presence of nanobubbles in the rough features.<sup>82</sup> Wallqvist and co-workers investigated two surfaces with nanoparticles of two different sizes disorderly distributed on the surfaces and provided the explanation of less restrictions for cavity growth on the smaller roughness length scale, hence giving forces of longer range and greater magnitude.<sup>55</sup> In a third study, Jung and Bhushan argue that the difference in adhesion force between nanostructures and microstructures is mainly due to the difference in contact area.<sup>83</sup> Previous findings in combination with the results obtained in this work lead to the following conclusions: If cavities are not formed, the adhesion force decreases with an increase in surface roughness/contact area. If the cavity is allowed to grow to its optimal size, the adhesion is independent of the surface roughness. If cavities form, but is restricted in their growth, the adhesion is less compared to a surface with very low roughness.

### 2.2.3 Adhesion

Cohesion and adhesion are two intimately connected terms where the first describes the internal energy needed to separate two bodies of the same material while the latter depicts the situation when two bodies of different materials in an intervening medium is to be separated. The work of adhesion can be calculated using

$$W_{\text{adh}} = \gamma_A + \gamma_B - \gamma_{AB} \quad (2-16)$$

where  $\gamma_A$ ,  $\gamma_B$  are the surface energies of two materials and  $\gamma_{AB}$  is the interfacial energy for the two materials in contact.<sup>84</sup> This equation describes the ideal case when the surfaces are perfectly smooth and in equilibrium. For real systems, parameters like roughness, humidity and surface charges make the situation more complicated. The measured adhesion can therefore be a combination of contributions from different types of forces such as van der Waals forces, chemical or hydrogen

bonding, capillary forces and steric forces, making interpretation very difficult. In this study, the observed adhesion between the surfaces is mostly explained by capillary forces but it cannot be excluded that other forces, like the van der Waals forces, have an influence as well.

Several different theories, developed from contact mechanics, describing the elastic deformation of samples exist. They can also be used to explain adhesion forces in colloidal systems. One of them is the Johnson-Kendall-Roberts (JKR) theory predicting

$$F_{\text{adh}} = 3\pi R\gamma_{\text{int}} \quad (2-17).^{85}$$

$F_{\text{adh}}$  is the adhesion force between the surface and the probe and  $\gamma_{\text{int}}$  is the interfacial tension. The JKR theory can be applied to systems with a large probe, a soft sample and with large adhesion between the surfaces.

## 2.3 Friction

Friction is an important phenomenon occurring between all surfaces moving relative to each other. As early as in the 15<sup>th</sup> century, Leonardo da Vinci performed studies demonstrating that the friction force,  $F_f$ , is proportional to the applied load,  $F_N$ , and independent of the macroscopic contact area. This was later rediscovered by Guillaume Amontons<sup>86</sup> leading to the empirical law of Amontons

$$F_f = \mu F_N \quad (2-18)$$

where  $\mu$  is the friction coefficient, which was later further developed by Charles-Augustin de Coulomb<sup>87</sup> who stated that the frictional force is also independent of sliding velocity. These, apparently simple, discoveries have proven very successful in predicting and studying friction between a range of different materials used in many applications. In general, smooth surfaces show a good correspondence with Amontons' law also on a microscopic or nanoscopic level.<sup>88-90</sup> For rough surfaces, the situation is more complicated and, as Bowden and Tabor pointed out, the true area of contact between two surfaces significantly differs from the apparent

area.<sup>91</sup> Recently, several studies have addressed the question whether these rules developed for macroscopic surface could be applied for surfaces exhibiting roughness length scales in the nano- or micrometer range. Several of them also found good correlations with the model law of Amontons.<sup>92-97</sup> However, for surfaces exhibiting strong adhesive forces, Amontons' rule is no longer valid. In a load versus friction plot, high adhesive forces are often seen as large hysteresis between the loading and unloading regime as well as a high force offset value,  $F^0$ . Derjaguin suggested that Amontons' law should instead read

$$F_f = \mu F_N + F^0 \quad (2-19)$$

in order to also account for the adhesive forces.<sup>27</sup> Several studies have tried to relate the measured friction to either adhesion hysteresis or the adhesion itself, but due to humidity and surface roughness effects it has proven challenging to obtain exact results.<sup>98-101</sup>

## 2.4 Wetting

The wettability, that is the behavior of a liquid on a solid substrate, is an important phenomenon both in nature and in many technical applications. As previously mentioned, plants and animals often exhibit special wetting behaviors such as the self-cleaning properties of a lotus leaf or the water-repellent wings of a butterfly. The wettability is often discussed in terms of the contact angle at which a liquid droplet meets the solid-vapor interface. A surface with a water contact angle below  $90^\circ$  is termed hydrophilic, above  $90^\circ$  it is hydrophobic and, as previously stated, above  $150^\circ$  it is termed superhydrophobic. In general, a more hydrophobic surface also has a lower surface energy while on a surface with high surface energy, the liquid spreads to a thin film. Young established the connection between the contact angle,  $\theta$ , and the surface tensions of the solid-liquid,  $\gamma_{sl}$ , solid-gas,  $\gamma_{sg}$ , and liquid-gas,  $\gamma_{lg}$ , interfaces through

$$\gamma_{sg} = \gamma_{sl} + \gamma_{lg} \cos \theta \quad (2-20)$$

as can be seen in Figure 2-4.<sup>102</sup>

The Young equation is valid for liquid droplets on a smooth solid surface. For a rough surface, the real contact angle may significantly differ from the apparent contact angle. There exist two main theories on how to predict and explain wetting on a rough surface; the Wenzel and the Cassie-Baxter models.

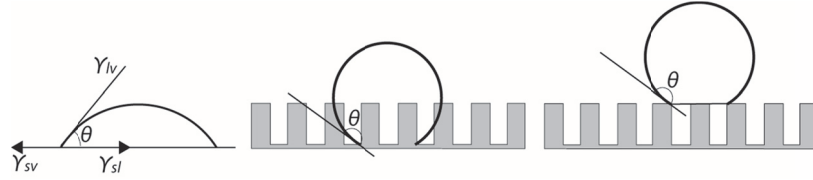


**Figure 2-4.** To the left, parameters relevant for Young's equation (Eq. 2-20) are displayed. In the middle, a water droplet on a rough hydrophobic surface with penetration of the surface features illustrates the Wenzel state while the image to the right, with a water droplet resting on top of the surface structure with air hidden underneath, shows the Cassie-Baxter state.

#### 2.4.1 Wenzel state

The Wenzel regime is described as the condition where the liquid fully penetrates the space between the roughness features resulting in complete wetting of the surface (Figure 2-4). The contact angle,  $\theta_{\text{real}}$ , on a rough surface, can, according to the Wenzel model, be related to the contact angle on a flat surface,  $\theta_{\text{flat}}$ , by,

$$\cos \theta_{\text{real}} = r \cos \theta_{\text{flat}} \quad (2-21)$$

where the roughness factor,  $r$ , gives the ratio between the real surface area and the corresponding projected surface area of a flat surface.<sup>103</sup> For a hydrophobic surface, energy is needed to wet the increased surface area created by the rough structures, hence increasing the contact angle compared to a smooth surface. For a hydrophilic surface, the situation is the opposite with a decrease in contact angle for a rough surface.

### 2.4.2 Cassie-Baxter state

In the Cassie-Baxter regime, air is trapped in the rough/heterogeneous surface features causing the liquid droplet to rest on top of an air layer as shown in Figure 2-4. This regime is associated with superhydrophobic surfaces exhibiting large roughness in combination with very low surface energy. The high interfacial energy between water and air leads to a higher contact angle on the rough than on the smooth surface. The contact angle of a heterogeneous surface with patches of different chemistry or wetting behavior can, according to the Cassie-Baxter model, be described by,

$$\cos\theta_{\text{real}} = f_1\cos\theta_1 + f_2\cos\theta_2 \quad (2-22)$$

where  $f_1$  and  $f_2$  are the area fractions of the two types of patches.<sup>104</sup>

### 2.4.3 Transitions between Wenzel and Cassie – Intermediate situations

In reality, surfaces often exhibit wetting behavior intermediate to those of the Wenzel and Cassie-Baxter models with partial liquid penetration of the rough structure. Also, studies have shown how transitions between the two clearly defined states are possible by, for example, simply changing the method with which the droplet is added to the surface<sup>105</sup> or by increasing the amount of ethanol in a water/ethanol mixture.<sup>106</sup> Another method is to put physical pressure on the droplet while it rests on the surface.<sup>107</sup> Clearly, the activation energy for transition between the states is low enough for this to occur.

### 2.4.4 Validity of the assumptions underlying the Wenzel and Cassie-Baxter models

An on-going debate, which had an upswing when Gao and McCarthy published their paper with the provocative title “How Wenzel and Cassie were wrong”,<sup>108</sup> discusses the validity of the Wenzel and Cassie-Baxter models. Several previous experiments had already shown how the Wenzel or Cassie-Baxter models failed to correctly predict the contact angle on many surfaces.<sup>109-113</sup> This seems to be the case when the droplet

covers chemical or topographical heterogeneities but still has its three-phase contact line over a homogeneous area. Recent studies have confirmed these observations suggesting that it is the nature of the surface at the three-phase contact line that decides the value of the contact angle making the situation beneath the droplet insignificant,<sup>114,115</sup> while others argue that the debate is all a consequence of incomplete interpretation of the equations or failure in performing the experiments correctly.<sup>116-119</sup>



## 3 Experimental

In this chapter, the main instruments and techniques used to perform the scientific studies reported in the thesis are presented.

### 3.1 Atomic force microscopy

The atomic force microscope (AFM) was introduced in 1986 by Binnig and co-workers.<sup>120</sup> At first, it was mainly used to image the topography of samples at a resolution of nanometer down to atomic scale, by moving a sharp tip in lateral direction over the surface. By the development of the colloidal probe technique, where a spherical probe or another object with a defined geometry is used to map the surface, force and friction measurements between surfaces using the AFM became increasingly used.<sup>121,122</sup> Lately, an increased interest to extract more parameters from the force curves resulting from every tip-surface interaction, has enabled new modes in which properties like adhesion, stiffness and electrical conductivity can be quantitatively measured with high lateral resolution.

The main principles of the AFM are illustrated in Figure 3-1. The sample is placed on top of a scanner which can move the sample and cantilever relative to each other in  $x$ ,  $y$  and  $z$  directions by the utilization of a piezoelectric material. A laser is focused on the backside of a cantilever, which is the part that senses the sample, and reflected onto a detector, often a split photodiode. The front side of the cantilever pointing towards the sample has either a sharp tip or a probe with another geometry that interacts with the surface. The interaction, whether it is attractive or repulsive, makes the cantilever deflect which changes the position of the reflected laser beam in the detector. The voltage output signal from the detector can be translated into height changes or forces.

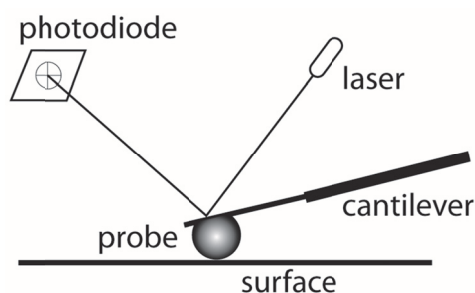


**Figure 3-1.** Schematic illustrating the principle of the AFM with a laser being focused on the back side of the cantilever with the attached probe and then further reflected onto the photodiode detector.

### 3.1.1 Imaging

Traditionally, the AFM has been used to study topography of surfaces by the recording of height images. Many different molecules and materials with differences in height scales have been studied through this technique. The resolution of the measurement is determined by the dimension of the small tip attached to the end of the cantilever. There exist different imaging modes like contact mode and Tapping mode® and the mode can be changed depending on the material and the type of information wanted. In contact mode, the tip and surface are always in contact by keeping the level of the detector response constant during imaging. Tapping mode® has, since long, been the most popular imaging tool due to its gentleness, making it possible to image soft and sensitive samples. The cantilever is oscillated at its resonance frequency and taps the surface gently. The trend in AFM imaging goes towards instruments and software that are easy to handle and provide a high level of automation. Recently, several new modes like the PeakForce QNM® from Bruker or the Pulsed force mode from Witec give the possibility to extract more details from the force curves. The previously recorded phase image from Tapping mode can now be resolved into several different parameters such as adhesion or surface deformation, providing more and also faster information compared to before.

### 3.1.2 Force

Normal forces between a tip or colloidal probe attached to the cantilever and the surface can be measured by moving them relative to each other in vertical direction. The poorly defined geometry of the tip normally used in imaging techniques makes it non-adequate for careful translation to forces. The development of the colloidal probe technique, where a spherical probe, a fiber or another object with a defined geometry is glued to the cantilever, has facilitated a precise determination of the measured force using the Derjaguin approximation (Eq 2-3)<sup>27</sup> and sphere/cylinder-flat surface interaction equations.

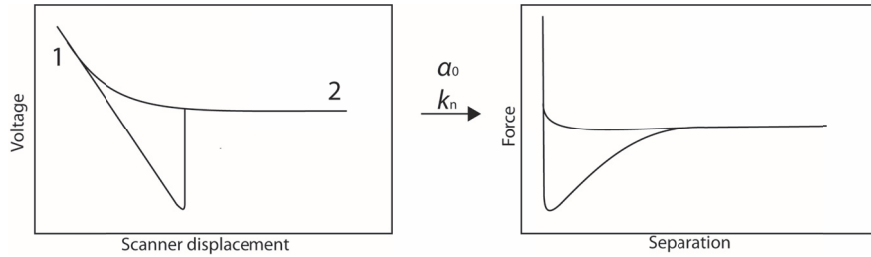


**Figure 3-2.** To the left, raw data from a normal force measurement with the cantilever deflection/voltage output plotted as a function of the scanner displacement in vertical direction. 1 indicates the region of the constant compliance and 2 the region of zero force. The image to the right displays a force separation curve obtained from modification of the raw data using the normal detector sensitivity ( $\alpha_0$ ) and the normal spring constant ( $k_n$ ).

Raw data from a normal force measurement are expressed as cantilever deflection in voltage against scanner displacement (Figure 3-2). Two regions of the force curve need to be located in order to translate the raw data into force as a function of probe-surface separation. The first is the constant compliance region defining the hard wall contact at which the probe and sample are in physical contact. The second one is defined as the region where no force is acting on the cantilever, hence called the region of zero force. The detector sensitivity,  $\alpha_0$ , as given by the slope of the constant compliance region is used together with the normal cantilever spring constant,  $k_n$ , to calculate the normal force.

Numerous methods to calibrate cantilevers have been proposed of which the Sader,<sup>123</sup> Hutter & Bechhoefer<sup>124</sup> and Cleveland<sup>125</sup> methods are the

most widely used. The Sader method has been used in this work and is based on the principle that the thermal motion of an object is damped by a viscous fluid. During calibration, the cantilever is allowed to vibrate freely at its resonance frequency due to thermal motion in air. The obtained frequency,  $f$ , and Q-value, which describes how damped the cantilever is *i.e.* how much energy loss that occurs, are used together with dimensions of the cantilever and the viscosity,  $\eta$ , and density,  $\rho$ , of the fluid to get the normal spring constant,  $k_n$ . When measuring cantilever motions in lateral direction, also the torsional spring constant,  $k_t$ , needs to be calibrated, and this is done similarly to what is described above.

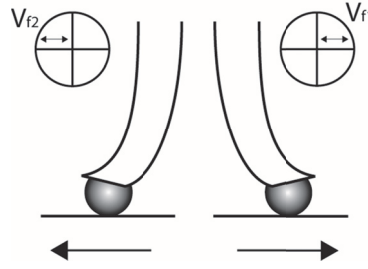


**Figure 3-3.** Schematic image of a probe in contact with a surface that is moved in lateral direction which makes the cantilever twist. The insets show how the reflection of the laser spots is changed in the split photodiode during a measurement.

### 3.1.3 Friction

As illustrated in Figure 3-3, friction between a colloidal probe and a sample can be measured by keeping the surfaces in contact at a known normal load and moving them in lateral direction. The friction will then make the cantilevers twist and change angle, resulting in a torsional adjustment in the photodetector. By scanning the probe back and forth, there will be a difference in detector signal,  $\Delta V_f$ , between the trace and retrace. This value is employed to convert the detector output to the frictional force,  $F_f$ , using:

$$F_f = \frac{\Delta V_f k_t}{2} \frac{1}{\delta h_{\text{eff}}} \quad (3-1)$$

where  $\delta$  is the torsional detector sensitivity and  $h_{\text{eff}}$  is the effective height, *i.e.* the diameter of the probe plus half the thickness of the cantilever.

The friction coefficient,  $\mu$ , is defined as the slope of the linear fit for friction as a function of applied load. To determine  $\mu$ , the measurement is started with the probe and sample out of contact followed by a stepwise increase, and then decrease, of the load.

### 3.1.4 Contact angle of colloidal probe

The method of measuring the contact angle of a single particle attached to a cantilever, called microsphere tensiometry, has been developed by Preuss and Butt<sup>126,127</sup> and the continued developments of particle-bubble interaction measurements using the AFM have been summarized by Johnson *et al.*<sup>128</sup> Dynamic contact angles are measured either by recording a force curve against a water droplet in air or an air bubble in water. From the force curve between the probe with radius,  $R$ , and the water droplet, the maximum adhesion force,  $F_{\text{adh}}$ , gives the advancing contact angle,  $\theta_a$ , according to

$$F_{\text{adh}} = 2\pi R\gamma \sin^2 \frac{\theta_a}{2} \quad (3-2)$$

while the receding contact angle,  $\theta_r$ , is given by the jump-in distance,  $D$ , from an approach force curve between the probe and an air bubble using

$$\cos \theta_r = \frac{R-D}{R} \quad (3-3).$$

The advancing and receding contact angles correspond to the macroscopic contact angles described below through the movement of the three-phase contact line over the surface. When receding, less and less of the particle surface is in contact with the liquid while during advancing, the particle is pulled out of the air bubble hence having an advancing three-phase contact line.

### 3.2 Confocal Raman microscopy

The combination of a confocal microscope with Raman spectroscopy gives a technique suitable for spectroscopic mapping of elements on a surface. Applications range from phase separation of liquids such as alcohol-water mixtures<sup>129,130</sup> to analysis of paper<sup>131,132</sup> and pharmaceutical products.<sup>133</sup>

In a confocal microscope, a lens or objective is utilized to focus a point-like light source onto a sample. The lens also focuses the image spot onto an aperture, whose size is chosen to only let the central part of the light pass through and reach the detector.<sup>134</sup> This enables the recording of three-dimensional images and a better image contrast in comparison to conventional light microscopy.

Raman spectroscopy is based on inelastic scattering of photons giving a frequency shift that provides information about vibrational, rotational or other low frequency transitions in a molecule.<sup>135</sup> An incoming photon can either be absorbed by the molecule it encounters, which causes a change in dipole moment that can be studied by infra-red (IR) spectroscopy, or induces a polarization in the molecule, which produces an electromagnetic scattered radiation of photons away from it. Most photons that scatter from the sample have the same frequency as the incident photons, giving rise to Rayleigh/elastic scattering. However, a small fraction of the photons is scattered at different frequencies, *i.e.* inelastic collisions between the photon and the molecule have changed the vibrational energy of the molecule, thus causing Raman scattering.<sup>134,136</sup>

In a confocal Raman microscope, a Raman spectrometer is attached to a light microscope. By using a microscope, the light can be focused on small spots of micrometer sizes, hence increasing the resolution and the collecting efficiency. A schematic image of a confocal Raman microscope is shown in Figure 3-4. A map of the different chemical components on a surface can be created by scanning the sample in *xy* direction, recording a Raman spectrum in every image pixel. The best

possible resolution that can be obtained in lateral direction is  $\sim 200$  nm and can be calculated using

$$\Delta x = 0.61\lambda/NA \quad (3-4)$$

where  $\lambda$  is the laser wavelength and NA the numerical aperture. The resolution in vertical direction is given by

$$\Delta z \geq \left| \frac{4.4n\lambda}{2\pi(NA)^2} \right| \quad (3-5)$$

and is often  $\sim 500$  nm.<sup>137,138</sup> Depth profiles are recorded by extracting a set of Raman spectra along a fixed horizontal axis. The full width half maximum (FWHM) is a term often used for determination of the spatial resolution for a confocal system.<sup>139,140</sup> It is defined as the extent of a function given by the horizontal line between two points at the curve located at half the maximum value of the curve. This means that two lines can be resolved if the distance between them are larger than the FWHM.<sup>141</sup> In this work, it was used to define the position of the surface when covered by different liquids.

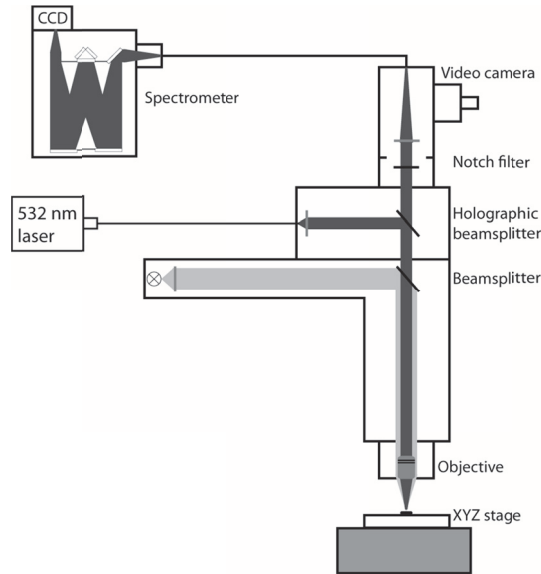


**Figure 3-4.** Schematic image of a typical confocal Raman microscope.

### 3.3 Contact angles

The sessile drop method is the most common way to measure the macroscopic contact angle of a surface. A drop is placed on the substrate of interest and its two-dimensional profile is recorded, often using a high resolution camera. The droplet baseline and shape are commonly analyzed by a program to get an exact value of the contact angle. Advancing and receding contact angles can be measured in two different ways; either by adding or removing liquid from the droplet with a syringe or by tilting the surface. Both methods depend on analyses of the contact angles when the droplet starts to move or roll over the surface. The contact angle hysteresis is given by the difference between the advancing and receding contact angles.

### 3.4 Surface preparation

Surfaces with the desired structure and properties were a prerequisite to be able to perform interpretable and reproducible force measurements. Today, there exist numerous methods to prepare structured surfaces of different sizes, morphology, wetting behavior and surface energies. The increased interest for fabrication of superhydrophobic surfaces during the last decade has led to the development of new methods as well as improvements of older ones.

#### 3.4.1 Langmuir-Blodgett

In order to prepare particle coated surfaces with a monolayer of particles and with the packing of particles as close to hexagonal as possible, Langmuir-Blodgett (LB) deposition was the method of choice. LB has, since long, been an established technique for deposition of amphiphilic molecules to prepare well-ordered monolayer surfaces.<sup>142-147</sup> The principle for deposition is described in Figure 3-5. The molecules or particles to be deposited are spread on a subphase in a Langmuir trough followed by compression of the barriers until a certain deposition pressure, *i.e.* a compact monolayer is reached. Surface pressure versus area ( $\pi$ - $A$ ) isotherms give information on the collapse pressure, and



indicate the area with large pressure changes where the deposition should be carried out. The molecules or particles are deposited onto the substrate either by lowering or raising the substrate from the subphase. The direction depends on the hydrophilicity and/or hydrophobicity of the molecules and substrate. Deposition of hydrophilic particles, like silica from a water subphase, demands adsorption of surfactant to the particles prior to spreading in the trough in order to control their hydrophilic/hydrophobic balance and prevent the particles from sinking.

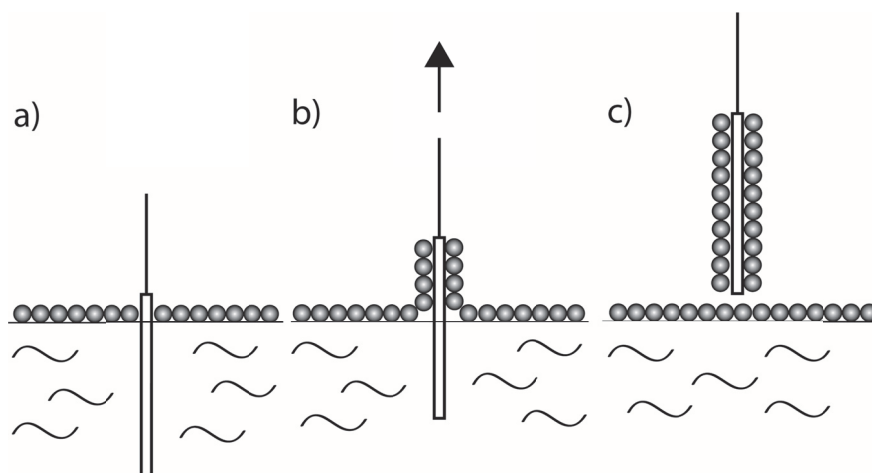


**Figure 3-5.** Principle of particle deposition using the LB technique. In a) particles are spread on the water subphase, in b) the substrate is slowly raised from the liquid while maintaining a constant deposition pressure and c) shows the resulting particle coated surface.

### 3.4.2 Lithography and etching

Lithography was used to prepare a pattern that acted as template during etching of pores in a surface. Several different lithographic techniques exist to create structures both in the nanometer as well as in the micrometer range. The most common for micrometer sized structures is photolithography, and this was the method used to prepare the surfaces used in this work. A promoter is often added to increase the adhesion between the substrate and the photoresist layer. The photoresist is applied to the substrate through spin coating to get a uniform layer with a thickness of a couple of micrometers. Light with varying intensities and

at different exposure times, is then used to create the desired pattern in the surface. This is followed by etching of the areas not protected by the photoresist, hence making a pattern in the underlying substrate. Several different etching techniques are available but here, deep reactive-ion etching using the Bosch process was employed to create the structures.<sup>148</sup> The plasma contains ions from sulfur hexafluoride ( $\text{SF}_6$ ) that etch the surface followed by passivation with octafluorocyclobutane ( $\text{C}_4\text{F}_8$ ) to get a protecting chemically inert layer. The number of etching and depositing steps as well as the time of each cycle can be adjusted to get the desired depth and structure of the pores.

### 3.4.3 Dip coating

A fast and easy approach to prepare surfaces with deposited particles, polymers or other molecules is sometimes required. Simple dip or drop coating techniques, where the molecules are subjected to a substrate either by repeated immersion of the substrate in a suspension or putting a droplet of the suspension on the surface and let it dry, are often efficient. Superhydrophobic surfaces, where a certain disorder and/or a roughness at different length scales often are required, are easily prepared in this way but also more structured surfaces where particles assemble on a surface by lateral capillary forces can be fabricated.<sup>149,150</sup> In this work, superhydrophobic surfaces were prepared by dip coating of glass substrates into a dispersion containing silica nanoparticles and a fluoropolymer creating a rough multilayered structure.

### 3.4.4 Sintering

The robustness of the surfaces was a major concern in this work, especially when using surfaces with particles that easily could be removed by touching them with an AFM tip or probe. A common way to make robust surfaces is by sintering at a temperature close to the melting temperature of, preferably, both the substrate and the deposited particles.

### 3.4.5 Silanization

Hydrophobization of the surfaces was utilized to receive the desired hydrophobic properties. Plasma polymerization<sup>151</sup> and thiolization<sup>152</sup> of gold are two well-established techniques to render a surface hydrophobic. However, since surfaces made of silica or silicon were utilized in the present work, silanization has been the main method used. The coupling reaction of attachment of silanes to an inorganic material is described in Figure 3-6. Surfaces like glass, silicon wafer and metal oxides can all be silanized due to their hydroxyl groups being able to displace the alkoxy group on the silane forming a  $\text{-Si-O-Si-}$  bond. The lower the surface energy of the surface, the more hydrophobic the surface becomes and therefore, a fluorocarbon based trifunctional silane, that can form cross-links across the surface, was used to prepare superhydrophobic surfaces. In the other studies, mono- or trifunctional hydrocarbon based silanes were used.

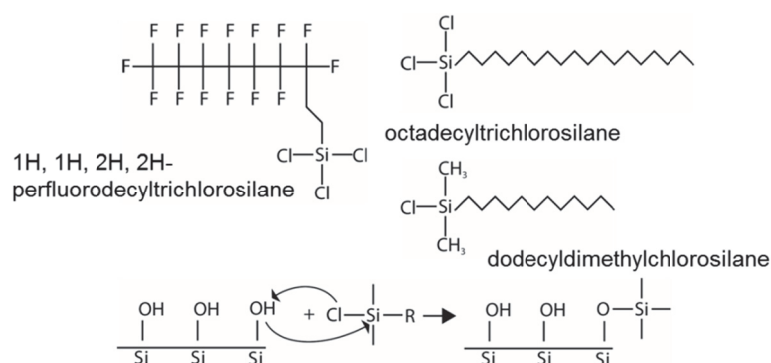


**Figure 3-6.** The silanes used in this thesis work and a schematic figure of the self-assembly of a silane to a glass or silicon surfaces.

## 4 Results

In this chapter, the main findings from the six papers included in this thesis are presented and discussed. The focus will be on summarizing the results and to create a cohesive picture of all studies. At first, the procedures utilized to prepare the three different types of surfaces, that is the particle coated surfaces, the pore array surfaces and the superhydrophobic surface, will be explained. This is followed by the results from the surface characterization process, including contact angle and confocal Raman measurements. The main part is then the summary of the results from the force measurements in which also the results from friction studies are discussed. The next section focuses on spectroscopic measurements on hydrophobic and superhydrophobic surfaces and removal of air cavities by addition of ethanol. The chapter ends by a discussion on the origin of interactions between hydrophobic surfaces, how they are affected by surface structures and different ways to predict them.

### 4.1 Surface preparation

Surfaces with defined and controllable structures and hydrophobic properties were a prerequisite to be able to study how surface interaction forces are affected by surface structure and roughness. This is why surfaces with very ordered structures consisting of monolayers of coated particles or pore arrays were prepared. In Figure 4-1, schematic figures of the particle coated and pore array surfaces can be seen. In some cases, the difference between hydrophobic and superhydrophobic surfaces was of interest, which demanded the preparation of superhydrophobic surfaces as well.

#### 4.1.1 Particle coated surfaces – Langmuir-Blodgett deposition

Particle coated surfaces, with silica particles having diameters of 30, 60, 90, 200, 800 and 4 000 nm, were prepared by Langmuir-Blodgett (LB)

deposition as further described in Paper II. Recording of surface pressure-area ( $\pi$ - $A$ ) isotherms in the Langmuir trough gave the surface pressure at which the monolayer of particles collapses. By preparing surfaces at three different deposition pressures and comparing the resulting particle packing, it was concluded that a deposition pressure of 30% of the collapse pressure resulted in a more defined structured surface compared to higher deposition pressures. At pressures of 60 and 90% of the collapse pressure, which previously have been used,<sup>153,154</sup> the particles showed a higher tendency to aggregate and deposit on top of each other.

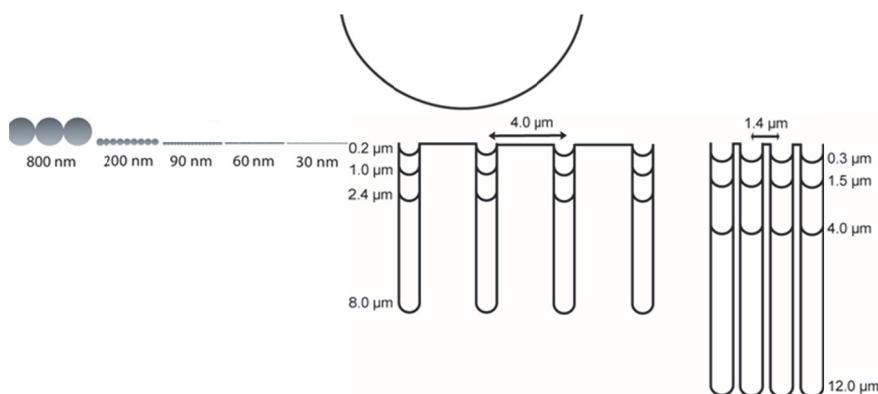


**Figure 4-1.** A schematic illustration of the particle coated surfaces and the pore array surfaces together with a typical colloidal probe used during force and friction measurements.

Initial deposition of particles gave well-ordered structures for the larger particles (200, 800, 4 000 nm) while the smaller particles (30, 60, 90 nm) showed large aggregates on the surfaces. Dynamic light scattering (DLS) experiments revealed that aggregates were present before spreading of particles in the trough, meaning that they were most probably formed in the solvent exchange process when water or isopropanol were replaced by chloroform. By filtration of the particle dispersions, the aggregates were removed and well-ordered surfaces could be prepared also for the smaller particles. An AFM image showing an example of a particle coated surface with 800 nm particles can be seen in Figure 4-2.

Sintering of the surfaces was performed in order to increase the robustness. Silanization, here in gas phase, rendered the surfaces hydrophobic.

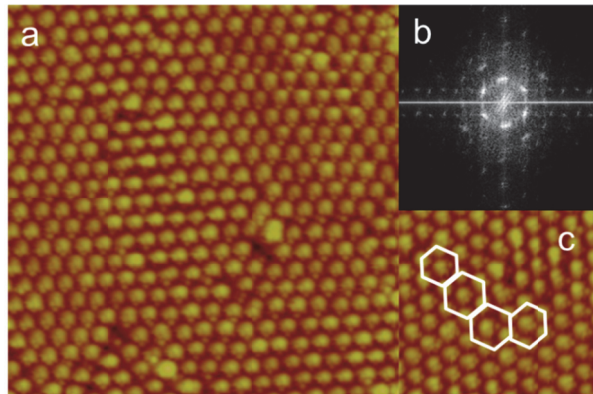


**Figure 4-2.** a) AFM image of a particle with 800 nm particles deposited using LB.  $15 \times 15 \mu\text{m}^2$  b) Fourier transformation of an AFM image with 800 nm particles, which shows a clear hexagonal pattern. c) The hexagonal markings show the pattern of particle arrangement on the surface.

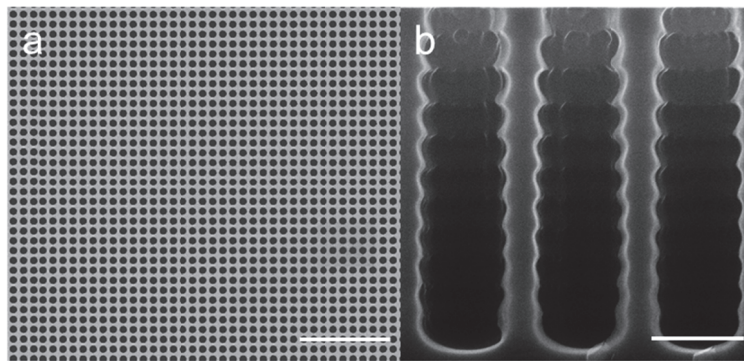


**Figure 4-3.** An example of a pore array surface with pore spacing of  $1.4 \mu\text{m}$  and a pore depth of  $4.0 \mu\text{m}$  recorded by high resolution scanning electron microscopy (HRSEM) where a) shows a top-view, scale bar:  $10 \mu\text{m}$ , and b) a side-view image, scale bar:  $1 \mu\text{m}$ .

#### 4.1.2 Pore array surfaces – Photolithography and etching

A photolithographic template was used to create a pattern consisting of circles with two different pore spacings,  $1.4$  and  $4.0 \mu\text{m}$ , on silicon

wafers. This was followed by etching with  $\text{SF}_6$  on the exposed areas to create pores followed by passivation with  $\text{C}_4\text{F}_8$  to stop the etching and give the pores a protecting layer. By varying the number of etching cycles, surfaces with different pore depths could be prepared. The two different pore spacings,  $1.4\ \mu\text{m}$  and  $4.0\ \mu\text{m}$ , were each obtained with four different pore depths;  $0.3$ ,  $1.5$ ,  $4.0$  and  $12.0\ \mu\text{m}$  for the first pore spacing and  $0.2$ ,  $1.0$ ,  $2.4$  and  $8.0\ \mu\text{m}$  for the latter. Top-view and side-view SEM images of a pore array surface are displayed in Figure 4-3.

For the pore array surfaces, hydrophobization by silanization was performed in liquid phase in a silane/toluene mixture.

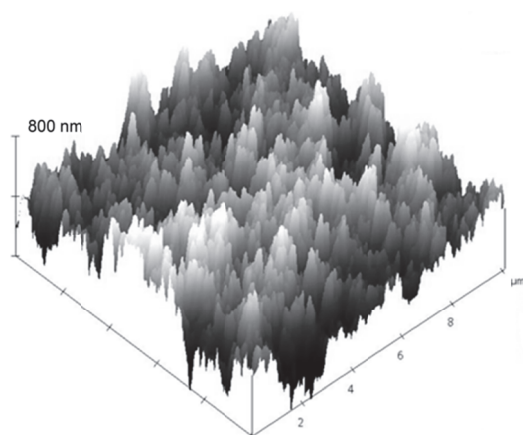


**Figure 4-4.** A superhydrophobic surface prepared by dip coating in a silica nanoparticle/fluoropolymer/fluorosolvent solution followed by silanization recorded by AFM imaging.

#### 4.1.3 Superhydrophobic surfaces – Dip coating

Repeated dip coating of glass substrates into a  $16\ \text{nm}$  silica particle/fluoropolymer/fluorosolvent formulation created a rough structure on both micro- and nanoscale according to a previously developed protocol.<sup>155</sup> Sintering was utilized to make these surfaces more robust, followed by silanization in gas phase to give the necessary low surface energy to make the surfaces superhydrophobic. An AFM image of a superhydrophobic surface is shown in Figure 4-4. As a reference

surface, a glass substrate was dip coated in a fluoropolymer/fluorosolvent mixture without nanoparticles followed by silanization, thereby producing a hydrophobic surface with similar chemical composition as the superhydrophobic one.

## 4.2 Surface characterization

Characterization of the surfaces in terms of their structure, roughness and wetting properties are crucial in order to develop an understanding of the unique situation at the different surfaces. A summary of the macroscopic water contact angles measured on all the different surfaces can be found in Figure 4-5.

### 4.2.1 Particle coated surfaces – Hexagonal structure and robustness

The particle coated surfaces needed to be robust and to have a defined surface roughness and structure in order to know that all parts of the surfaces behaved homogeneously during measurement series. Information about the structure was mainly provided by the recorded AFM images but also contact angle measurements were used to elucidate the particle packing. The most optimal packing for spherical particles on a surface is hexagonal close-packing. Fourier transforms of the AFM images revealed a short-range hexagonal order but disorder on a longer scale. An example of an image of a surface with 800 nm particles with an average particle to particle distance of 874 nm can be seen in Figure 4-2b. Roughness analysis of the AFM images gave experimental  $R_a$  values, which were compared to theoretical values calculated using the equations proposed by Oudrhiri-Hassani and co-workers<sup>156</sup> and based on hexagonal packing. The theoretical values were higher than the experimental ones and the difference was larger for the smaller particles. This observation is suggested to not only be a consequence of the more disordered structure of the smaller particles, but also of the AFM tip not being sharp enough ( $R$  approx. 3 nm) to precisely probe the area between the small particles which is discussed in more detail in Paper II.



After hydrophobization, macroscopic water contact angles were measured on all the surfaces. As expected, the increased roughness on a particle coated surface compared to a flat glass substrate gave an increase in contact angle from  $108^\circ$  for the flat surface to  $120\text{-}124^\circ$  for the particle coated surfaces (Figure 4-5). No trend in contact angle with respect to particle size could be detected; hence the wetting degree is the same for particles in the micrometer size range as well as for nanoparticle smaller than 100 nm. The roughness factor,  $r$ , as included in the Wenzel equation (Eq. 2-21) can be calculated from the contact angle measured on a particle coated surface compared to the value measured on a flat surface. The theoretical value,  $r = 1.9$ , was calculated by combining hexagonal geometry and a hemispherical model.<sup>157</sup> The experimental roughness factors varied between 1.62 and 1.81, *i.e.* again indicating short-range hexagonal order but also the occurrence of a slight longer-range disorder. To calculate  $r$ , one must assume the surfaces to be in the Wenzel wetting regime which means the surfaces would be completely wetted. This seems likely for the large open areas between the top parts of the particles. However, the narrow cavities at the bottom part of the volume between the particles could contain air pockets, which would create a small degree of Cassie-Baxter state in this area. The packing density and the theoretical roughness factor suggest that approximately 95% of the area is wetted (Wenzel state) while the remaining 5% consist of air being trapped close to the surface (Cassie-Baxter state). Hence, the experimental roughness factors could be used to conclude that also contact angle measurements suggest a local order and a long-range disorder due to slight discrepancy from the theoretical value. It has been shown that, in order to induce a complete transition in the wetting regime from Wenzel to Cassie-Baxter state for particle coated surfaces, multilayers of particles in the micrometer size range with at least one layer of nanoparticles on top, are necessary.<sup>22</sup>

To test the robustness of the surfaces after sintering, an AFM tip was moved in contact mode over the surface and AFM images were recorded on the same spot before and after testing of the robustness. The pressure at which the surfaces were tested was chosen to be 2 GPa. This was

proven to be high enough to tell whether the surfaces would stay the same during the force and friction measurements. After careful examinations of several different sintering temperatures and times it was found that, in order to create a good robustness, both the particles and the substrate had to start melting together. In conclusion, sintering should preferably be carried out at a temperature close to the melting temperature of the particles and the substrate, which means using the same material for both is advantageous. More information on preparation and analysis of the particle coated surfaces can be found in Paper II.

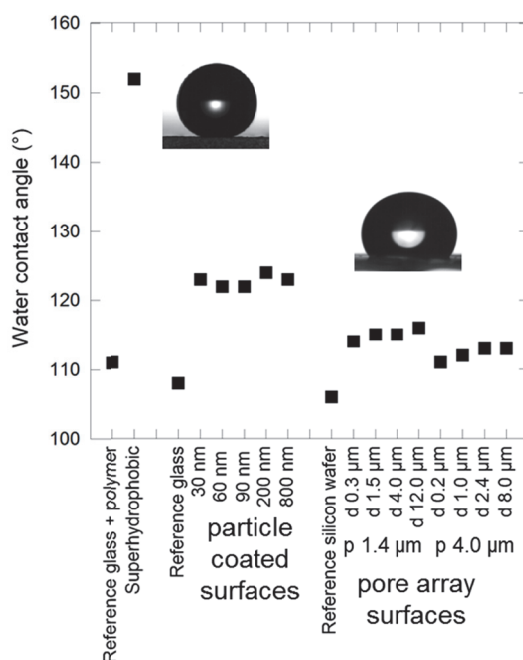


**Figure 4-5.** Summary of static water contact angles on all the hydrophobic surfaces. The surfaces termed 30-800 nm are the particle coated surfaces and the surfaces presented to the right are the pore array surfaces. p = pore spacing, d = pore depth

#### 4.2.2 Pore array surfaces – Structure of three-phase contact line and water penetration into the pores

Macroscopic contact angles with water and different concentrations of ethanol in water were measured on the hydrophobized pore array surfaces

(Figure 4-5). In comparison to a flat reference surface, the contact angles on both the surfaces with 1.4  $\mu\text{m}$  and 4.0  $\mu\text{m}$  pore spacing had increased. However, no trend in contact angle with respect to pore depth was found, neither for water nor ethanol droplets. The contact angles were, in general, a bit higher on the surfaces with the smaller pore spacing which could be due to the larger amount of pores and therefore a more bent three-phase contact line. Theoretical contact angles were calculated using the widely used equations by Wenzel (Eq. 2-21) and Cassie-Baxter (Eq. 2-22). However, the Wenzel equation was not possible to use due to a too large extra area provided by the pores which would give a cosine of the angle out of range. The Cassie-Baxter model gave both water and water/ethanol contact angles that were larger than the experimental values by around 5°. As mentioned in section 2.4.4, the validity of the models has been seriously questioned. Several studies have shown the insignificance of heterogeneities underneath the droplet and suggested the situation at the three-phase contact line to determine the contact angle.<sup>108,109,113</sup> The discussion regarding this matter contains arguments in favor of the models suggesting a too small size of the liquid droplets in relation to the surface structures<sup>158</sup> and they propose the usage of local instead of global values of the roughness ratio.<sup>116</sup> The results from the present study confirm the need for a critical approach when using the Wenzel and Cassie-Baxter equations. Since the models did not predict an accurate result, the situation at the three-phase contact line was investigated by recording light microscopy images displayed in Figure 4-6. They revealed a jagged line with water wetting between the pores, while the 1:1 water/ethanol and the ethanol droplets behaved differently showing straight three-phase contact lines and no wetting in-between each pore.

Sliding angles, that is the tilting angle at which the liquid droplet first starts to move, were also collected and the droplets were studied during sliding. No significant difference between the surfaces was noted but the sliding angles were higher, 45° compared to 35°, with 20% ethanol than with water droplets. This could be compared to a sliding angle of 15° measured on the flat reference surface. The droplet movements over the pore array surface were not smooth but more step-like. It seemed like the

front of the droplet was pinned at one side of a pore followed by a sudden jump to the next pore. Also the shape of the receding part of the droplet was changing during movements across the different pores.

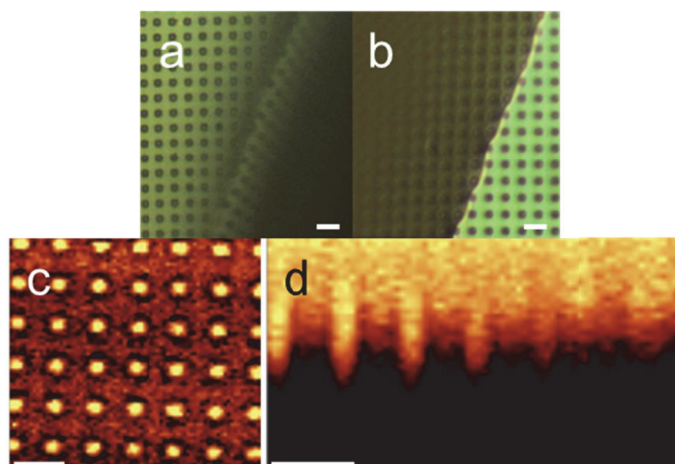


**Figure 4-6.** Liquids on a hydrophobic pore array surface with a pore spacing of  $4.0\ \mu\text{m}$  and a pore depth of  $8.0\ \mu\text{m}$ . a) A light microscopy image with a water droplet and b) an ethanol droplet showing that the water three-phase contact line is jagged and seems to avoid the pores while ethanol wets the surface in straighter lines. c) A top-view and d) a side-view confocal Raman image of the surface covered with water where water is seen as yellow and has clearly penetrated into the pores. Scale bars:  $5\ \mu\text{m}$

Even though the contact angle and the shape of the three-phase contact line are of interest, the situation underneath the droplet is of major importance for the forces between the surfaces and a colloidal probe. To further investigate the wetting behavior in and above pores covered by a liquid, confocal Raman microscopy images and Raman spectra were recorded. At first, water was added to the surface with a microscope glass slide on top giving a liquid film of approximately  $10\ \mu\text{m}$ . Images were recorded both in  $xy$  and  $xz$  directions. The images displayed in Figure 4-6 clearly show water penetration into the pores. This is somewhat surprising since water should not be able to go into pores having this size and a contact angle higher than  $90^\circ$  according to capillary theory.<sup>159</sup> It was speculated whether this observation is due to a different chemistry in the pores originating either from a lower amount of OH groups that could be silanized or incomplete removal of the  $\text{C}_4\text{F}_8$  passivation layer after

etching, making the silanization process less efficient. To make sure the silane had access to the pores during silanization, confocal Raman images were recorded with toluene (in which the silanization procedure was carried out). The images showed that toluene could easily penetrate into the pores and that silane had indeed been in contact with the pore walls. More information on these wetting studies using water can be found in Paper V.

#### 4.2.3 Superhydrophobic surface – Lotus effect

As already mentioned, the surface roughness, measured from AFM images, for the superhydrophobic surface was much larger, about 100 times, compared to a flat surface but also around 15 times larger than the particle coated surfaces with a monolayer of nanoparticles. This increase in roughness gave a water contact angle of around  $152^\circ$  on the superhydrophobic surfaces, which decreased to  $105^\circ$  for a 1:1 water/ethanol mixture and to  $22^\circ$  for pure ethanol. The surfaces exhibited the lotus effect with extremely low roll-off angles for water droplets.

### 4.3 Force measurements

A typical force-distance curve measured between hydrophobic surfaces in aqueous solution has many characteristic features as discussed in Section 2.2.2 and an example is displayed in Figure 4-7. On approach, no interaction between the surfaces is observed until there is a sudden on-set of attraction which makes them jump together. The distance, in this case approximately 25 nm, is referred to as the jump-in distance. The shape of the approach curve can vary and both smooth and continuous curves as well as discontinuous jumps towards the surface have been observed before.<sup>43,47,55,71</sup> When the surfaces start separating, the maximum adhesion force is observed as a minimum in the force curve. As described in the theory section, the features of this force curve can be interpreted by formation of an air cavity causing a strong attraction between the surfaces on approach. On retraction, the cavity is extended and breaks at a certain position, called the rupture distance. In the studies presented here, the adhesion force, the jump-in distance and the rupture distance were

statistically analyzed. In Paper V, the rupture force is also discussed. Force curves measured between flat hydrophobic surfaces can often be fitted to Eq. 2-14 assuming capillary forces between the surfaces. Force measurements between the structured surfaces presented below were always accompanied by measurements between a flat hydrophobic surface to establish the consistency of the results and compare the values to a reliable reference surface.

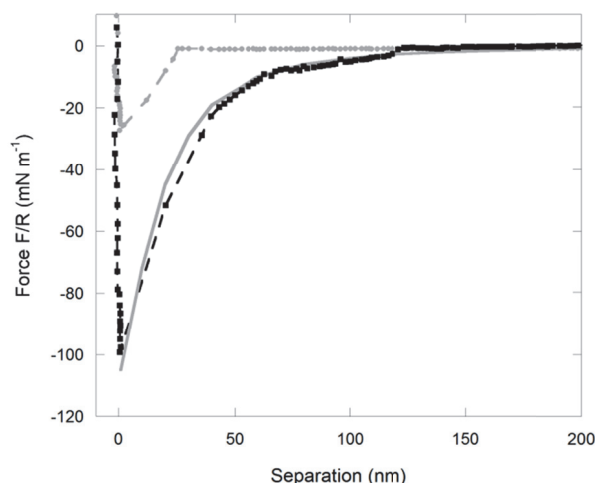


**Figure 4-7.** An example of a force curve measured between a flat hydrophobic surface and a hydrophobic colloidal probe. The solid grey line is a theoretical fit to Eq. 2-14. The grey broken line is the approach and the black broken line is the retract curve.

#### 4.3.1 Particle coated surfaces – Dependence on roughness length scale and extremely long-range forces

Forces were measured between all the particle coated surfaces prepared by LB deposition except the 4 000 nm particles; their polydispersity and a size similar to the probe made measurements difficult. The resulting force curves measured on different spots on the surfaces were analyzed in terms of their shape and statistical values. Both statistics and the shape of the force curves gave indications of the occurrence of two different mechanisms during a measurement series. Most of the force curves had the normal shape presented in Figure 4-8a, but there were also curves

displaying extremely long-range forces with jump-in distances of several hundreds of nanometers, rupture distances in the micrometer range and a retract curve indicating an increase in capillary volume during separation (Figure 4-8b). A closer analysis revealed an increased abundance of the long-range force curves the smaller the particles on the surface. For measurements with 30 nm particles, almost 30% had the long-range appearance while the fraction was 0.5% for 800 nm particles. The reference measurements with a flat surface displayed only the normal type of force curves which proved that neither the probe, liquid medium nor anything else in the experimental set-up was responsible for this unusual behavior. Instead, the reason behind must be found within the particle coated surface structure. The two different types of force curves, from now on referred to as Population 1 for the normal type and Population 2 for the long-range type, were split into two groups and their statistical occurrence was analyzed separately.

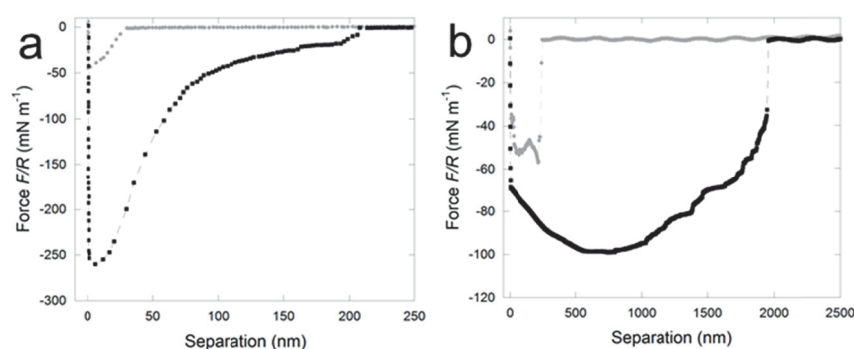


**Figure 4-8.** Representative force curves measured between a hydrophobic particle coated surface, in this case with 30 nm particles and a hydrophobic colloidal probe. a) Shows the normal type of force curve often seen for hydrophobic surfaces, here called population 1 and b) shows the extremely long-range interaction distance type of force curves (population 2) that closely resembles force curves measured between superhydrophobic surfaces. grey line = approach curve, black line = retract curve

Statistics from the force measurements with the particle coated surfaces displaying the Population 1 force curve appearance are summarized in Figure 4-9. As clearly seen, the trend is that both the adhesion force and the interaction distances are larger the smaller the particles on the surface.

This is true for the 30, 60 and 90 nm particles while there is very little difference between the 200 and 800 nm particles. Interestingly, the flat reference surface displays values intermediate to that of the particle coated surfaces. This suggests that a certain surface roughness promotes cavity formation, possibly due to excess air within the structure, but if the roughness is too large, pinning of the three-phase contact line between the large particles decreases the adhesion force and makes the cavity more unstable and easier to break. Possibly, the shape of the cavity can be altered to find an optimal contact angle for growth if the cavity has a certain roughness to rest on. The larger height difference for the larger particles also provides energy barriers for the movement of the cavity over the surface.

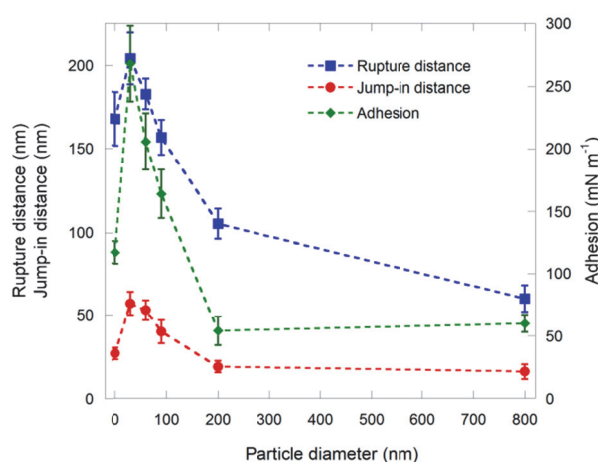


**Figure 4-9.** Summary of statistical values obtained from force measurements between a hydrophobic colloidal probe and the hydrophobic particle coated surfaces. Only values from Population 1 force curves can be seen here. In general, the adhesion force and the interaction distances are increased when the particle diameter on the surface is decreased.

Mean values calculated from all of the force curves assigned to belong to Population 2 showed, in contrast to Population 1, no trend with respect to particle size. The adhesion force, jump-in and rupture distance varied enormously from one measurement to another. For example, rupture distance values could range from approximately 800 nm up to 2.5  $\mu\text{m}$ . Also, due to the very few Population 2 force curves recorded for several



of the surfaces, reliable statistics were not obtained. When discussing the reason for formation of the Population 2 force curves, the first thing that comes to mind is its similarity to force curves measured between superhydrophobic surfaces.<sup>155,160</sup> Superhydrophobic surfaces are known to be in the Cassie-Baxter state with a large reservoir of air underneath the water droplet. As concluded from the wetting studies and mentioned in the discussion about Population 1 force curves above, the particle coated surfaces display a slight degree of Cassie-Baxter wetting with trapped air between the particles. This excess amount of air is most likely a prerequisite for Population 2 curves to form, providing an in-flux of air when retracting the probe during a measurement. Already on approach there is a profound difference between the two populations. The on-set of attraction starts at a larger separation distance for the Population 2 force curves and they often show a sharper jump to lower forces with some repulsive steps in-between. This can be interpreted as air bubbles being present on top of the roughness features and the steps are then a consequence of the deformation of the bubble during approach. This would also explain why Population 2 force curves are more frequently appearing for the smaller roughness length scales; an air bubble of around 100 nm can easily rest on top of the 30 nm particles but for the larger particles, it is more likely they will be found in the crevices between particles. Hence, air nanobubbles found on the particles in combination with the air reservoir found between and beneath the particles are the reasons this type of force curves is seen. Paper III provides further discussion about forces on the particle coated surfaces.

#### 4.3.2 Pore array surfaces – Consequences of pores observed in the force curves

Force measurements were performed with all the different hydrophobic pore array surfaces against a hydrophobic colloidal probe by recording force curves at different spots on the surface. Again, many of the force curves displayed the normal characteristics seen in Figure 4-7, but there were also force curves showing larger rupture forces, as defined as the force at the position where the cavity breaks, and sometimes several steps in the curve during retraction were observed as illustrated in Figure 4-10.

To avoid confusion with the different force curves measured with the particle coated surfaces, these curves are divided into Group 1, corresponding to the normal type, and Group 2 displaying large rupture forces/steps in the curve.

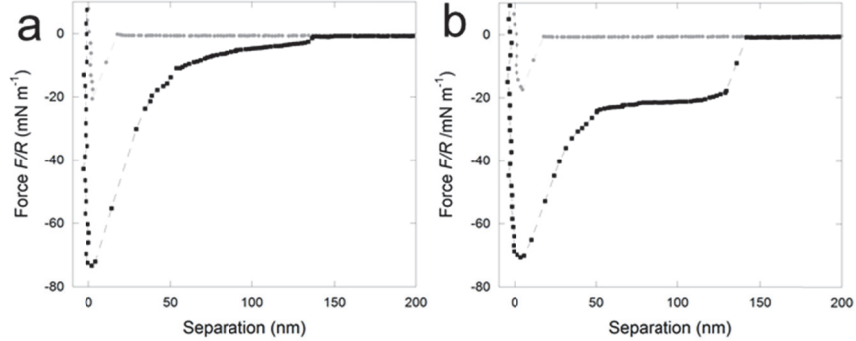


**Figure 4-10.** Representative force curves measured between a hydrophobic pore array surface, in this case a surface with a pore spacing of  $1.4 \mu\text{m}$  and a pore depth of  $4.0 \mu\text{m}$ , and a hydrophobic colloidal probe. Grey shows approach curves and black shows measurements on retraction. a) Shows a normal type of force curve, most likely with the cavity resting on a flat part of the surface while in b) the cavity is thought to come in close contact to a pore which makes it break at a large rupture force.

Curve fitting of Eq. 2-14 to Group 1 force curves indicated a cavity radius of about 800 nm just before the start of retraction of the probe. This means that it is sometimes possible for the cavity to avoid being in contact with a pore, and as seen in the images of the three-phase contact line, the contact line does avoid the pores if possible. Thus, Group 1 force curves are thought to correspond to measurements on a flat reference surface, while the Group 2 force curves, which never occur on the flat reference surface, are interpreted as being measured in close proximity to a pore. This seems likely when examining the percentage of Group 2 force curves in comparison to the area covered by the pores which are very similar. Group 2 force curves are more common for the surfaces with  $1.4 \mu\text{m}$  pore spacing; it is less likely that the cavity avoids the pores when the pores are closer together. The shape of the force curve in Figure 4-10b can be explained by pinning of the three-phase contact line at a pore edge causing a distortion in the cavity during retraction. This will

force the cavity to break at a distance where it is not fully extended, hence the large attractive force at the rupture distance.

The shape of the force curves, especially the Group 2 force curves, can also give information about the situation in the pores covered by water. In some cases, the colloidal probe must be positioned precisely above a pore. If the pores had been completely filled with water, as the Raman measurements suggest they are, no air cavity could have formed. Since such cavities always were observed, small amounts of air have to be present at the bottom of the pore or around the pore walls.

The statistical values extracted from the force curves from the two groups were analyzed separately, and the results are shown in Figure 4-11. For all parameters, the Group 1 curves show a closer resemblance to the reference surface but, obviously, the pores affect the measured values also when they do not change the shape of the force curve. Since measured forces are higher and interaction distances generally are larger for the reference, it seems like the pores hinder cavity formation to a greater extent than they promote it. This means they provide an energy barrier for cavity growth in a similar way as was concluded for the larger particles during measurements on the particle coated surfaces. As seen in Figure 4-11, the jump-in distance increases with a decrease in pore depth for both pore spacings. This is likely a consequence of a shorter distance for evaporated water or air inside the pores to travel to the surface, hence making it easier to assemble and form a cavity. For the rupture distance the situation is reverse, here the distance instead decreases with a decrease in pore depth. The rupture distance is, to a large extent, determined by the amount of air available in the cavity during retraction. That is why, even though the cavity has difficulties to form when the pores are deep, as soon as it is formed, the deeper pore can provide the cavity with more air as it is being extended. This parameter is the only one where values for some of the surfaces exceed that of the reference surface, which is another indication of larger amount of air leading to larger cavities. The interpretation of the trends in adhesion force is a challenge since the adhesion is affected by several different parameters such as contact area and structure around the pores or the pore wall and it

is not obvious which play the most important role. For further discussion about force measurements on the pore array surfaces, see Paper V.

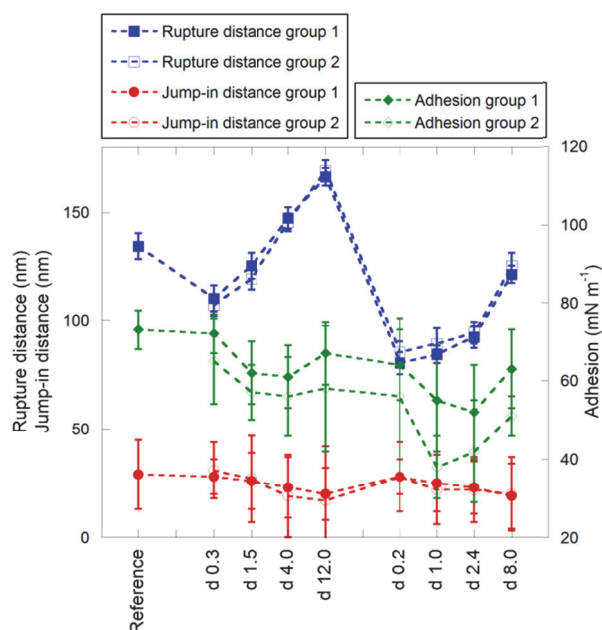


**Figure 4-11.** Summary of force measurement statistics between a hydrophobic colloidal probe and the hydrophobic pore array surfaces.  $d$  = pore depth

### 4.3.3 Superhydrophobic surfaces – Long-range forces

The special characteristic of the superhydrophobic surfaces used here is a disordered structure which creates a large surface roughness. The rough features provide excellent capabilities for air trapping that can function as an air reservoir when covered with water. Just as described above for the particle coated surfaces, these superhydrophobic surfaces give rise to force curves with extremely long-range interactions. In contrast to the monolayer surfaces, these long-range forces are seen for all force curves measured on the superhydrophobic surface. This is likely due to its higher contact angle and the mixture of roughness features on both the macro- and nanoscale, creating many pockets that can provide the cavity with air. A typical example of such a force curve is displayed in Figure 4-12. It shows an increase in cavity volume during retraction; hence air moves

towards the cavity and makes it grow. This means that the capillary force model described above (Eq. 2-14) is not applicable to this system. It is suggested above that these long-range forces are associated with nanobubbles. The first study showing these long-range interactions between superhydrophobic surfaces was also looking for air bubbles on the surface.<sup>160</sup> They did not find any and argued that cavitation is a consequence, not of air, but of evaporation of confined water between the surfaces. Importance of surfaces roughness was, however, emphasized in line with this study.

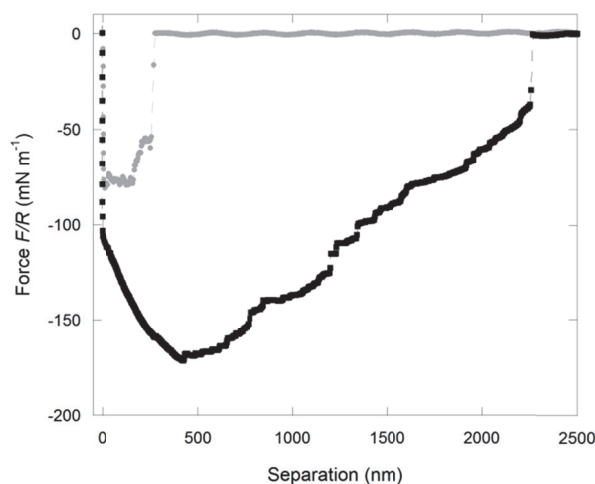


**Figure 4-12.** A typical force curve measured between a superhydrophobic surface and a hydrophobic colloidal probe. Note the extremely large interaction distances and the increased cavity volume during retraction (black curve).

## 4.4 Friction measurements

Friction measurements were performed using only the particle coated surfaces. In contrast to the other studies, measurements between hydrophilic surfaces were also done in order to investigate both the influence of surface structure and surface chemistry.

#### 4.4.1 Particle coated surfaces – Amontonian or adhesion controlled friction

The particle coated surfaces were also used in friction measurements using a hydrophilic surface against a hydrophilic probe, and a hydrophobic surface against a hydrophobic probe in aqueous solution. Measurements started with the probe out of contact and followed by an increase and later a decrease in the applied load. Raw data values with friction force as a function of measurement time clearly displayed probe motion over the particles on the surface (Figure 4-13a) which was more evident the larger the particles. For the hydrophilic surfaces, a plot of the frictional force against the applied load exhibited straight lines both on increased and decreased load as can be seen in Figure 4-13b, which is in accordance with Amontons' empirical law (Eq. 2-18). However, the force offset value ( $F^0$ ), *i.e.* the friction at zero load, was for all particle coated surfaces a bit higher than zero which would indicate the slightly modified Amontons' rule (Eq. 2-19), which also considers the sometimes present adhesion force, to be valid in this case. There is a weak trend of a higher  $F^0$  for larger particles on the surface. The friction coefficient,  $\mu$ , was higher for the particle coated surface compared to the flat reference surface, but showed no variation with respect to particle size. Therefore, it was suggested that the relative surface geometry, *i.e.* the similar local asperity slope on all particle surfaces, and not the surface roughness determines the friction in this case.

The change in surface chemistry from hydrophilic to hydrophobic by the addition of a silane layer was accompanied by an increase of the measured friction force. Also, the mechanisms responsible for the forces were clearly changed. On increasing load, there was still a weak linear dependence between the friction and the load. However, when the load was decreasing, the friction could sometimes increase as can be seen in Figure 4-13c.  $F^0$  values were also much larger for the hydrophobic surfaces compared to the hydrophilic ones. As previously seen in the normal force curves measured between hydrophobic surfaces, there is always a large adhesion between the surfaces which explains the high  $F^0$  value. Accumulation of air between the probe and the surface during a friction measurements cause large adhesive properties also when the load

is decreased. An important energy dissipative mechanism contributing to the friction force is suggested to be shear-induced motion of the cavity across the surface. Paper IV gives a more detailed discussion about the frictional forces.

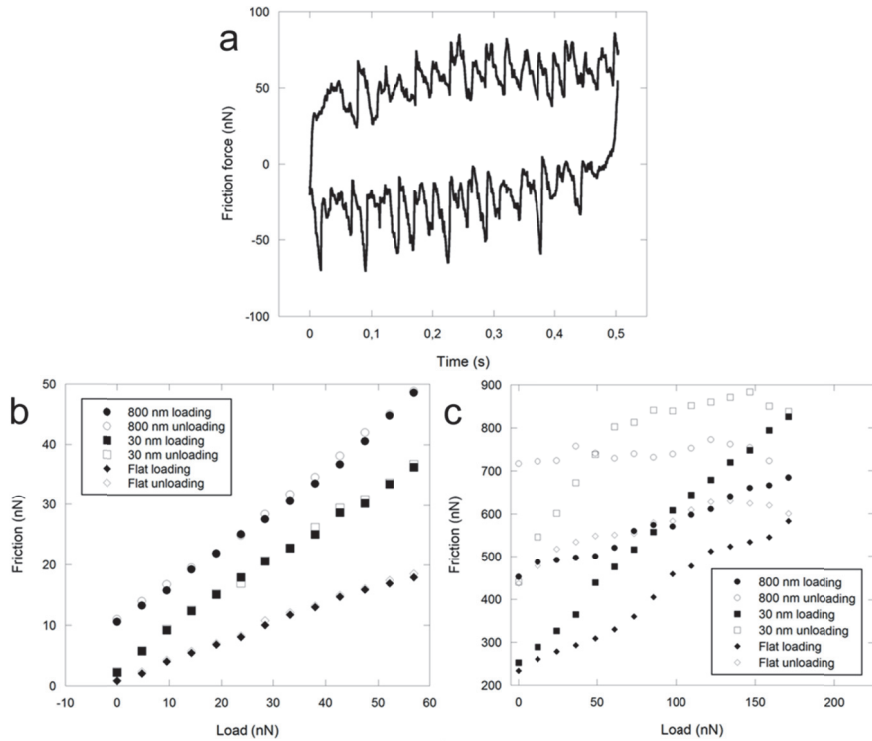


**Figure 4-13.** a) Raw data from friction measurements between hydrophilic surfaces in aqueous solution. This plot shows a particle coated surface with 800 nm particles. b) Friction against load data between hydrophilic surfaces which follow Amontons' law and show that the particle coated surface exhibits a steeper slope, *i.e.* a higher friction coefficient compared to the flat reference surface. c) Friction against load data for measurements between hydrophobic surfaces where a large adhesion between the surfaces are seen as a large force offset value and hysteresis between the loading and unloading curve.

## 4.5 Capillary effects

Here, results related to the phenomena exhibited by hydrophobic surfaces are highlighted and discussed. A combination of results from spectroscopic and force measurements is presented.

#### 4.5.1 Detection of air/water vapor and accumulation of ethanol on superhydrophobic surfaces

As further described in Paper I, superhydrophobic and flat hydrophobic surfaces were covered with water or a 1:1 water/ethanol mixture and imaged using confocal Raman microscopy. The results were evaluated in terms of a depth profile from a fixed  $xy$  position in the image. The normalized intensity of each peak collected from the spectra was plotted against the depth and the full width half maximum (FWHM), that defined the position of the surface, was used to judge whether liquid penetration into the surface or depletion from the surface occurred. Figure 4-14a shows how ethanol has accumulated close to and even penetrated into the superhydrophobic surface more than water. This is in contrast to an experiment with a hydrophobic surface where no difference between water and ethanol in liquid penetration depth into the surface is detectable. However, it is easy to believe that there is a difference between water and ethanol also on the hydrophobic surface, but at a much smaller scale than on a superhydrophobic surface and therefore below the resolution limit (approx. 500 nm) of the instrument.

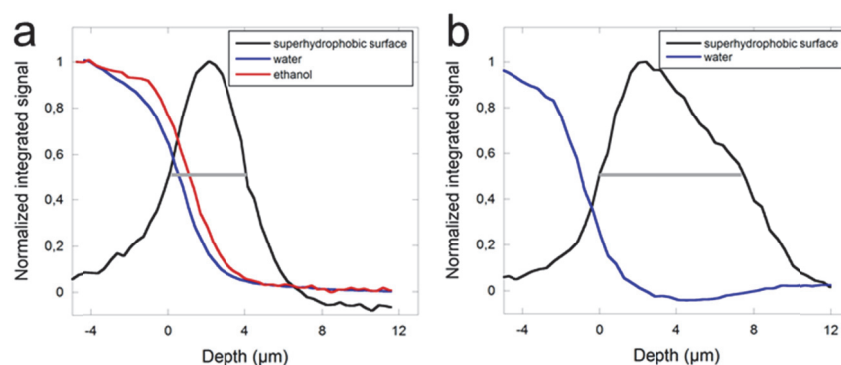


**Figure 4-14.** Raman depth profiles showing a superhydrophobic surface covered with a) a water/ethanol mixture and b) water. At the surface defined by the FWHM (grey line), water is clearly depleted from the surface while for the water/ethanol mixture it is evident that ethanol wets the surface better than water does and aids wetting also by water. For the hydrophobic surface (not shown here) neither water depletion nor accumulation of ethanol at the surface were detectable. The peaks used to decide the change in intensity when going from the liquid bulk to the surface were for the surface  $714\text{ cm}^{-1}$ , water  $3330\text{ cm}^{-1}$  and ethanol  $870\text{ cm}^{-1}$ .



Raman measurements in pure water also showed a small penetration of liquid into the hydrophobic surface. However, for the superhydrophobic surface, water was clearly depleted from the surface leaving an interfacial volume where no or very weak Raman signals were obtained (Figure 4-14b). Since air is not dense enough to give Raman signals, capillary evaporation and accumulation of air in the rough surface features are likely reasons behind this observation. Comparing Raman spectra for bulk water to that of water in close proximity to the superhydrophobic surfaces, the peaks at 1 635 and 3 240  $\text{cm}^{-1}$  turned out to be stronger for interfacial water. The peak at 3 240  $\text{cm}^{-1}$  corresponds to hydrogen bonded water as shown by vibrational sum frequency spectroscopy (VSFS) which indicates more structured water close to the surface.<sup>161-163</sup> This finding is surprising considering the limited depth resolution in confocal Raman spectra and would need further investigations to be clarified.

#### 4.5.2 Influence of ethanol – removal of capillary forces

In order to study the removal of capillary forces and further investigate the accumulation of ethanol on hydrophobic surface, force measurements on the pore array surfaces in water/ethanol mixtures of different ratios were performed. 5, 10, 15 and 20 vol% of ethanol were studied by rinsing of water injected into the AFM liquid cell in-between every ethanol measurement. As seen in the force curve displayed in Figure 4-15a, the shape of the curves changes remarkably in presence of ethanol. The jump-in distance and the adhesion force decrease with added ethanol and the lack of cavitation makes the retract curve jump directly to zero force after detaching from the surface. Further, very small traces of ethanol, probably accumulated in the pores, were difficult to remove during water rinsing and the presence of ethanol affects the in-between measurements with water as seen in Figure 4-15b. The jump-in distance and the adhesion force display the original value measured in water before the very first addition of ethanol but the rupture distance remains at zero just like in ethanol mixtures, indicating that no cavity or a very unstable cavity that immediately ruptures, is formed. Hence, very small amounts of ethanol remaining in the pores have a profound effect on the stability of the cavity. For the flat reference surface, ethanol was easily removed

and the measurements in water after previous measurements in ethanol regained the same appearance as the very first measurement.

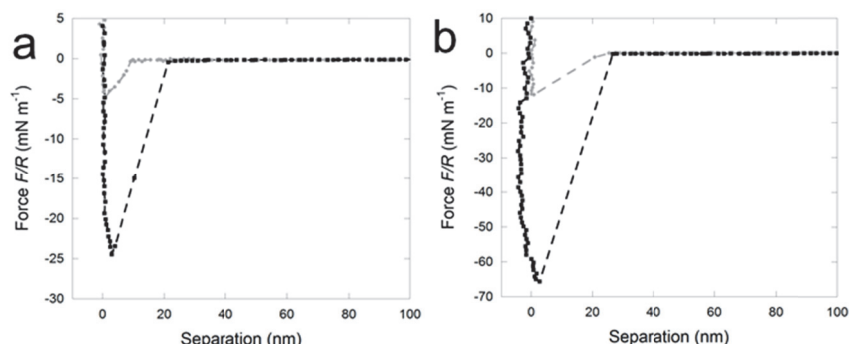


**Figure 4-15.** Force curves obtained from measurements with a hydrophobic pore array surface using a pore spacing of  $1.4\ \mu\text{m}$  and a pore depth of  $12\ \mu\text{m}$ . In a) the measurement was performed in a 5% ethanol solution and b) shows measurements in water after previous measurements in water/ethanol mixtures. Even though the jump-in distance and the adhesion force are higher in the measurement with water, the cavity, if any, ruptures immediately upon separation. Experimental points in grey is during approach, black during retract.

As seen in previous confocal Raman measurements, ethanol wets a hydrophobic surface and removes the air layer close to the hydrophobic surface. The observed forces measured in water/ethanol mixtures can thus not be a consequence of air cavity formation between the surfaces which means that other types of forces must be involved. One suggestion for the observed attractive interactions is van der Waals forces, which always are present between surfaces. To investigate this, the experimentally recorded force curves were compared to theoretically calculated van der Waals forces using Eq. 2-9 and the Hamaker constants for the silica surfaces across different water/ethanol liquid media. The force curves measured on approach had, for all ethanol concentrations, a larger on-set of attraction distance than the theoretical values. The same result was obtained by comparing the distance at which the slope of the theoretical force curve equals the spring constant of the cantilever used to measure the interactions. This information indicates that van der Waals forces cannot be solely responsible for the measured interactions. Capillary forces originating from capillary condensation of ethanol instead of air

cavitation is suggested to be the most likely explanation for the observed forces which is further discussed in Paper VI.

## 4.6 General discussions about interactions between hydrophobic surfaces

The evidence for air being present close to a superhydrophobic surface obtained from confocal Raman measurements is crucial for many of the conclusions from the previously presented force measurements, providing new insights on the origin of the observed forces between hydrophobic surfaces. There have been studies showing both direct and indirect evidence of air close to the surface but this study is unique in the sense that very long-range effects could be detected by spectroscopy.<sup>66,69,70</sup> Superhydrophobic surfaces gave the most distinct effects on the interfacial liquid, displaying the most long-range forces, the largest air/water vapor layer and an accumulated layer of ethanol. It is therefore reasonable that similar interfacial events occur also at hydrophobic surfaces but that the resolution of our confocal Raman instrument is too low to detect the layer. Additionally, the thickness of air/vapor/ethanol layers probably decreases in conjunction with the hydrophobicity of the surface.

The question whether it is an air layer on the hydrophobic surface or if air is present in the form of nanobubbles on the surface is often discussed in the literature on long-range force, but has not been a main focus of this project. Previous studies looking specifically for nanobubbles have either proven their existence or found no evidence for such small bubbles.<sup>58,63,67,160,164</sup> The main controversy of the nanobubbles is their size being too small to be stable for more than a short period of time according to Laplace pressure theory. Despite this, they have been shown to exist for much longer time periods and a study by Wennerström has shown how dissolved gas can substantially prolong the lifetime of the bubbles.<sup>165</sup> As discussed in the section on long-range force curves, the large jump-in distance and the repulsive features in the approach force curve indicated the presence of bubbles deformed by the colloidal probe.

However, the Raman images show a more continuous layer with very weak Raman signals, interpreted as air or water vapor, close to the surface. The resolution of the Raman image is probably the limiting factor and even though single bubbles would exist on the surface, the instrument would have difficulties resolving them. An observation favoring the theory on air layers over nanobubbles is that in-flux of air to the cavity seems to be crucial during many of the performed measurements. A continuous air layer would provide easier access if all air is connected compared to the situation where they are split into single bubbles.

Another important aspect of interaction forces between hydrophobic surfaces is its dependence, or lack of dependence, on surface hydrophobicity. Several studies have provided evidence for an increase in the range and magnitude of the measured forces as a consequence of increasing the hydrophobicity of the surfaces.<sup>80,81</sup> However, most of the previous studies have been performed on flat surfaces or on surfaces with a disordered structure. The studies in this thesis clearly show that surface hydrophobicity provide very little information about the quantitative values extracted from the force curves. Instead, there seems to be several other important factors facilitating cavity formation and growth. The free energy of the system is generally lowered by the formation of a cavity in close proximity to hydrophobic surfaces. For smaller roughness length scales or shallower pores, less water and air are required in order to form the cavity due to smaller volume and easier access to air. The surface roughness is important due to its ability to confine air within the rough features. As seen for the particle coated surfaces, with higher forces and rupture/jump-in distances on the particle coated surfaces compared to the reference, a certain roughness on the surfaces facilitates cavity growth. However, when the surface roughness is too large, it is difficult to transport air hidden between the particles to the cavity. It was not possible to determine a critical roughness at which the cavity formation is hindered instead of facilitated compared to a reference surface. The  $R_a$  roughness parameter for the 200 and 800 nm particles is much smaller than the value measured on a superhydrophobic surface, which clearly displays much longer forces and interaction distances. Instead, a mixture

of roughness and the ability of the surface to transport air are likely the critical parameters. Even though the contact angles are higher on the pore array surfaces compared to the reference, this is not accompanied by larger forces and the pore structures often seem to counteract cavity growth. Since the area around the pore edges is the same for all the pore array surfaces, it is reasonable to believe the qualitative influence from the pores, for the same pore spacing, is similar on all of them. Hence, the differences between the pore depths are likely due to, again, access of air. Another reason is the energy barriers presented by the pores and the height differences on the particle coated surfaces with the larger particles. These energy barriers for movement of the three-phase contact line over the surface decrease the range and magnitude of the measured forces.

All the force measurements performed on the different surfaces provided valuable information on how to increase or decrease forces between structured hydrophobic surfaces. It is not possible to present a complete theory predicting exact quantitative values, but a qualitative behavior can be foreseen by looking at the following surface properties: The first to take into account is the actual structure; does it contain features able to function as air reservoirs? The access is also important, a very deep pore could certainly host large amounts of air but it might be difficult to provide it to the cavity. The length scale of the roughness features is another important parameter. As long as the surface is not superhydrophobic, the best approach is to compare this length scale to the expected diameter of the cavity. A too large roughness length scale in relation to the dimensions of the cavity would hinder formation due to the escape routes given in the structures, but also prevent movement of the three-phase contact line and cavity growth. These rules can be applied when looking at other common types of surface structures not investigated here, such as pillars or pyramidal shapes. A pillar structure of a low energy material would exhibit superhydrophobic behavior as investigated by He *et al.*<sup>166</sup> and Park *et al.*<sup>24</sup> This would most likely generate the long-range type of force curves previously seen for superhydrophobic surfaces. However, it has been difficult to find trends in forces and jump-in/rupture distances for this type of force curves and formation and growth seem to be completely uncorrelated events. It is not

possible to say whether this would be the case also for structured superhydrophobic surfaces with, for example, different spacings between the pillars as well as different heights. For pyramidal shapes, having more open structures, the length scale of the features would be critical. Large structures could disturb the formation of a cavity and create energy barriers during growth while a small length scale could possibly facilitate cavity formation just like the case for the particle coated surfaces. However, the structures might be too open to give access to a large amount of excess air. A similar approach could be applied to predict ranges and magnitudes of forces between hydrophobic surfaces also displaying other types of surface structures.

## 5 Conclusions

This thesis highlights important aspects of surface structures and properties in relation to hydrophilicity/hydrophobicity/superhydrophobicity of the surfaces and interaction forces between such surfaces. Using confocal Raman microscopy, accumulation of air/water vapor was observed in close proximity to a superhydrophobic surface providing evidence for cavitation during force measurements between hydrophobic surfaces. This observation served as a foundation in the following studies which focused on the influence of surface structure on the forces. This required preparation of surfaces with a defined structure and, hence, surfaces with hexagonally close-packed particles were prepared. Roughness analysis and Fourier transforms of AFM images as well as contact angle measurements suggested a local order but a slight disorder on a longer length scale. It was concluded that the surfaces exhibited almost complete wetting but still with some air hidden between and beneath the particles. Surfaces with pore array structures displayed a jagged three-phase contact line and presence of water in the pores with air most likely present around the pore walls and at the bottom of the pores.

Force measurements with particle coated surfaces resulted in two different populations of force curves showing very different appearances. Population 1 force curves had the normal shape most often seen for hydrophobic surfaces with a retract curve that was possible to fit to capillary force theory. Statistical analyses showed a decrease in range and magnitude of the forces with an increase in surface roughness length scale, *i.e.*, an increase in particle size. This was attributed to easier access of air and lower energy barriers for cavity formation for the smaller particles. Force curves measured on flat reference surfaces displayed forces in-between those of the particle coated surfaces suggesting that a certain surface roughness facilitates cavitation while a too large roughness hinders it. The Population 2 force curves displayed extremely long-range forces with rupture distances exceeding micrometers and an

increase in cavity volume during retraction. Due to the similarity to force curves measured on a superhydrophobic surface, it was concluded that air bubbles resting on top of the particles and an in-flux of air to the cavity during separation were the explanations for this long-range force.

Friction measurements between hydrophilic surfaces showed good correspondence to Amontons' rule with a linear dependence on load both during an increase and decrease of the applied load. The calculated friction coefficients were found to increase going from a flat surface to a particle coated surface but stayed approximately the same for all particle sizes. A change in surface chemistry from hydrophilic to hydrophobic was discovered to completely change the measured friction forces with large adhesion forces being present in the hydrophobic case.

The pore array surfaces also showed different force curve appearances with the possibility to directly see the influence of the pores in some of them. The normal type of force curves was sorted into Group 1 while force curves displaying large rupture forces or discontinuities in the retraction curve were assigned to belong to Group 2. Group 1 curves were suggested to have been measured on a flat part of the surface while Group 2 curves are suggested to be recorded in close proximity to pores with the pores causing sudden ruptures of the cavity or pinning of the three-phase contact line. When looking at the mean values extracted from the force curves, the jump-in distance increases with a decrease in pore depth while the situation is the reverse for the rupture distance. In a shallow pore, air is closer to the surface, hence making it easier for the cavity to form. As soon as the cavity is created, a deeper pore can provide more air which gives a longer rupture distance.

When water/ethanol mixtures were used as liquid medium during force measurements on the pore array surfaces, cavitation of air did not occur, as shown by the retract curve going directly to zero force after the surfaces were separated. Instead, capillary condensation of ethanol is thought to be the main reason for the observed interactions in presence of ethanol. It could be concluded that very small amounts, even traces, of



ethanol were enough to remove cavitation. Accumulation of ethanol at the surface and in the pores is likely the reason behind this observation.

Clearly, surface structures have a profound influence on interaction forces between hydrophobic surfaces. For structured surfaces, in contrast to smooth, it is evident that the hydrophobicity of the surfaces cannot solely be used to explain the measured forces and interaction distances. The results obtained in this project suggest that it should be possible to give qualitative theoretical predictions of the forces between structured hydrophobic surfaces with respect to the type of structure and the length scale of the structural features.

## 6 Future work

During the progress of this project many ideas on interesting experiments have been suggested. Unfortunately, there has not been enough time to investigate all of them and therefore some of the studies with the ability to give further information in relation to the discoveries made within the context of this work, are presented in this chapter.

The most obvious experiment would be to look at the summaries on how to predict forces between structured surfaces and investigate whether the predictions are correct. As discussed in the results chapter, surfaces exhibiting pillar structures or pyramidal shapes could be studied. It would be especially interesting to investigate if it is possible to find trends in the range and magnitude of the force curves for structured surfaces in the Cassie-Baxter regime. So far, it was suggested that the range and magnitudes of the long-range force curves seen for superhydrophobic surfaces are completely random. By using for example pillar structures with different heights and spacing, this could be further investigated.

The study of friction was not started until the end of this project and there was not enough time to investigate the dependence on surface structure in detail. It is evident that surface structures have a huge influence on friction forces. Despite the importance of friction both in every-day life as well as in industry, there are still only a few studies done on friction at the nanoscale. Measurements between superhydrophobic surfaces in different media could give valuable information on how the supposed air layer and its removal affect frictional forces. Also, friction on the pore array surfaces would be interesting to study in order to see if they follow the traditional Amontonian behavior.

Wetting and liquid penetration are two phenomena only briefly studied in this project. This could be continued using different types of liquids and also by modifying the surfaces in different ways using, for example different silanes providing charged surfaces. Particles deposited in

multilayers instead of a monolayer on a substrate could be used as model surfaces when studying imbibition of liquids in a porous layer.

Many questions still remain regarding forces between superhydrophobic surfaces. One possible approach could be to study cavitation between superhydrophobic surfaces using the surface force apparatus (SFA). In contrast to the AFM, the SFA can be utilized to give the position of the underlying substrate as well as to visually detect air/water vapor in the cavity. This was tried very quickly using the superhydrophobic surface prepared by dip coating but it was not transparent enough to be applied in the SFA. There exist several recipes describing how to prepare transparent superhydrophobic coatings and one of them could possibly be tested.

Another way to study fundamental properties of hydrophobic surfaces would be through variation of the hydrophobicity of both the surface and the colloidal probe. By using the microsphere tensiometry technique described in 3.1.4, also the contact angle of a single probe attached to the cantilever can be measured. This means that similar/different/higher/lower contact angles of the surface in relation to the probe could be used during force measurements.

## 7 Acknowledgements

There are numerous people who have helped and supported me throughout the years and I would here like to take the opportunity to thank some of them.

First, I would like to express my sincere gratitude to my supervisor Prof. Per Claesson. The inspiring attitude and the valuable scientific input you always provide have been a great help and comfort during this project. I would also like to warmly thank my second supervisor, Prof. Agne Swerin. Thank you for giving a person who, five years ago, knew very little about surface forces the opportunity to work in this project but thanks also for scientific guidance and for involving me in other projects at YKI. My unofficial third supervisor Assoc. Prof. Esben Thormann is gratefully acknowledged for patiently teaching me how to use the AFM and for always taking the time to discuss results, papers and to answer all my stupid questions.

Omya Development AG is gratefully acknowledged for providing the funding for this project. Prof. Pat Gane and Dr. Joachim Schoelkopf are thanked for support, for all interesting and challenging discussions as well as for showing great enthusiasm about the project.

My coauthors on all the papers are acknowledged for making the different projects possible. Lisa Skedung and Prof. Mark Rutland are thanked for good collaboration on the particle coated surfaces. I am very thankful to Yashar Hormozan and Prof. Jan Linnros for sharing your very nice pore array surfaces with us. Dr. Birgit Brandner is thanked for doing the confocal Raman measurements and Martin Wählander for excellent skills in developing the protocol to prepare the superhydrophobic surfaces.

Prof. Hans-Jürgen Butt and Dr. Michael Kappl are thanked for inviting me to come to the Max Planck Institute for Polymer research in Mainz and for teaching me the colloidal probe contact angle measurements.

Of course, I would like to thank everybody at YKI who has created a nice working environment and made these last, almost five, years both enjoyable and rewarding. I would like to recognize Mikael Sundin and Rodrigo Robinson for excellent help in the lab. Dr. Viveca Wallqvist is thanked for making my life easier by doing such a great job in the first Omya funded project. All past and present Ph.D. students, but especially Anna, Carina, Christian, Lisa, Hanna, Asaf, and Lina, are thanked and remembered for lunches, after works and for pleasant discussions. A special thank you goes to Hanna, Lina and Josefina for always being willing to listen to my complaints and for all the long talks about everything that is important in life.

All the people I have come in contact with at the Division of Surface and Corrosion science at KTH are thanked for help, discussions and for nice company during courses.

Mina vänner utanför jobbet och alla mina släktingar förtjänar ett varmt tack för allt stöd under åren. Mamma och pappa är värda ett enormt tack för att ni alltid ordnar allt så bra, för att ni alltid hjälper till och för att ni alltid trott på mig. Mikaela och Rebecka ska ha tack för att man alltid kan höra av sig till er, för att ni (nästan) alltid är på bra humör och för att ni står ut med er besserwisser till storasyster. Mormor och morfar har en väldigt stor del i att det blev en doktorsavhandling skriven. Tack för all uppmuntran att läsa och studera samt för all tid ni ägnade åt att leka skola och alla andra konstiga lekar jag hittade på.

Christian, I could go on forever thanking you for all the help with practical issues regarding this thesis and at home, for tolerating my bad mood and for always trying to cheer me up. YKI will be a very empty place without you and not seeing your green Lync dot on Monday Nov 5 will force me to fight back some tears. That day, like every other day, I will be infinitely happy and thankful that I get to meet you at home.

## 8 References

- 1 Barthlott, W. & Neinhuis, C. *Planta* **1997**, 202, 1-8.
- 2 Neinhuis, C. & Barthlott, W. *Annals Of Botany* **1997**, 79, 667-677.
- 3 Feng, L., Zhang, Y., Xi, J., Zhu, Y., Wang, N., Xia, F. & Jiang, L. *Langmuir* **2008**, 24, 4114-4119.
- 4 Bhushan, B. & Nosonovsky, M. *Philosophical Transactions of the Royal Society A: Mathematical, Physical and Engineering Sciences* **2010**, 368, 4713-4728.
- 5 Gao, X. & Jiang, L. *Nature* **2004**, 432, 36-36.
- 6 Wanasekara, N. D. & Chalivendra, V. B. *Soft Matter* **2011**, 7, 373-379.
- 7 Polymenidou, M. & Cleveland, D. W. *Journal of Experimental Medicine* **2012**, 209, 889-893.
- 8 Head, M. W. & Ironside, J. W. *Neuropathology and Applied Neurobiology* **2012**, 38, 296-310.
- 9 Ma, M. & Hill, R. M. *Current Opinion in Colloid & Interface science* **2006**, 11, 193-202.
- 10 Gnedenkoy, S., Sinebryukhov, S., Egorkin, V., Mashtalyar, D., Alpysbaeva, D. & Boinovich, L. *Colloids and Surfaces A: Physicochemical and Engineering Aspects* **2011**.
- 11 Boinovich, L., Gnedenkoy, S., Alpysbaeva, D., Egorkin, V., Emelyanenko, A., Sinebryukhov, S. & Zaretskaya, A. *Corrosion Science* **2011**.
- 12 Kulinich, S. & Farzaneh, M. *Langmuir* **2009**, 25, 8854-8856.
- 13 Tourkine, P., Le Merrer, M. & Quéré, D. *Langmuir* **2009**, 25, 7214-7216.
- 14 Huang, L., Chen, K., Lin, C., Yang, R. & Gerhardt, R. A. *Journal of Materials Science* **2011**, 46, 2600-2605.
- 15 Stanssens, D., Van den Abbeele, H., Vonck, L., Schoukens, G., Deconinck, M. & Samyn, P. *Materials Letters* **2011**.
- 16 Ma, M. L., Mao, Y., Gupta, M., Gleason, K. K. & Rutledge, G. C. *Macromolecules* **2005**, 38, 9742-9748.
- 17 Ma, M., Hill, R. M. & Rutledge, G. C. *Journal of Adhesion Science and Technology* **2008**, 22, 1799-1817.
- 18 Drelich, J., Nalaskowski, J., Gosiewska, A., Beach, E. & Miller, J. D. *Journal of Adhesion Science and Technology* **2000**, 14, 1829-1843.
- 19 Polat, M., Polat, H. & Chander, S. *International Journal of Mineral Processing* **2003**, 72, 199-213.

- 20 Wallqvist, V., Claesson, P. M., Swerin, A., Schoelkopf, J. & Gane, P. A. C. *Colloids and Surfaces A: Physicochemical and Engineering Aspects* **2006**, 277, 183-190.
- 21 Bravo, J., Zhai, L., Wu, Z., Cohen, R. E. & Rubner, M. F. *Langmuir* **2007**, 23, 7293-7298.
- 22 Tsai, P. S., Yang, Y. M. & Lee, Y. L. *Nanotechnology* **2007**, 18.
- 23 Ming, W., Wu, D., van Benthem, R. & de With, G. *Nano letters* **2005**, 5, 2298-2301.
- 24 Park, J., Lim, H., Kim, W. & Ko, J. S. *Journal of Colloid and Interface Science* **2011**, 360, 272-279.
- 25 Martines, E., Seunarine, K., Morgan, H., Gadegaard, N., Wilkinson, C. D. W. & Riehle, M. O. *Nano letters* **2005**, 5, 2097-2103.
- 26 Zhang, J. H. & Yang, B. *Advanced Functional Materials* **2010**, 20, 3411-3424.
- 27 Derjaguin, B. *Kolloid Zeits* **1934**, 69, 155-164.
- 28 Derjaguin, B. & Landau, L. *Acta Physicochimica URSS* **1941**, 14, 633-662.
- 29 Verwey, E. J. W., Overbeek, J. T. G. & Van Nes, K. *Theory of the stability of lyophobic colloids: the interaction of sol particles having an electric double layer*. (Elsevier New York, 1948).
- 30 Keesom, W. *Physikalische Zeitschrift* **1921**, 22, 129-141.
- 31 Debye, P. *Physikalische Zeitschrift* **1920**, 21, 178-187.
- 32 London, F. *Zeitschrift für Physik* **1930**, 63, 245.
- 33 Hamaker, H. C. *Physica* **1937**, 4, 1058.
- 34 Bradley, R. S. *Philosophical Magazine* **1932**, 13, 853.
- 35 de Boer, J. H. *Transactions of the Faraday Society* **1936**, 32, 0010.
- 36 Lifshitz, E. M. *Soviet Physics JETP* **1956**, 2, 73.
- 37 Visser, J. *Reports on the Progress of Applied Chemistry* **1968**, 53, 714.
- 38 Neumann, A., Omenyi, S. & Van Oss, C. *Colloid & Polymer Science* **1979**, 257, 413-419.
- 39 Israelachvili, J. N. *Intermolecular and surface forces*. (Academic press, 1991).
- 40 Gouy, G. *Journal of Physics* **1910**, 9, 457-467.
- 41 Chapman, D. L. *The London, Edinburgh, and Dublin Philosophical Magazine and Journal of Science* **1913**, 25, 475-481.
- 42 Israelachvili, J. & Pashley, R. *Nature* **1982**, 300, 341-342.
- 43 Israelachvili, J. & Pashley, R. *Journal of Colloid and Interface Science* **1984**, 98, 500-514.
- 44 Pashley, R. M., McGuiggan, P. M., Ninham, B. W. & Evans, D. F. *Science* **1985**, 229, 1088-1089.

- 45 Christenson, H. K. & Claesson, P. M. *Science* **1988**, 239, 390-392.
- 46 Rabinovich, Y. I. & Derjaguin, B. *Colloids and Surfaces* **1988**, 30, 243-251.
- 47 Parker, J. L., Claesson, P. M. & Attard, P. *Journal Of Physical Chemistry* **1994**, 98, 8468-8480.
- 48 Carambassis, A., Jonker, L. C., Attard, P. & Rutland, M. W. *Physical Review Letters* **1998**, 80, 5357-5360.
- 49 Froberg, J. C., Rojas, O. J. & Claesson, P. M. *International Journal of Mineral Processing* **1999**, 56, 1-30.
- 50 Christenson, H. K. & Claesson, P. M. *Advances in Colloid and Interface Science* **2001**, 91, 391-436.
- 51 Attard, P. *Advances in Colloid and Interface Science* **2003**, 104, 75-91.
- 52 Meyer, E., Rosenberg, K. & Israelachvili, J. *Proceedings of the National Academy of Sciences* **2006**, 103, 15739.
- 53 Wallqvist, V., Claesson, P. M., Swerin, A., Schoelkopf, J. & Gane, P. A. C. *Langmuir* **2007**, 23, 4248-4256.
- 54 Thormann, E., Simonsen, A. C., Hansen, P. L. & Mouritsen, O. G. *Langmuir* **2008**, 24, 7278-7284.
- 55 Wallqvist, V., Claesson, P. M., Swerin, A., Ostlund, C., Schoelkopf, J. & Gane, P. A. C. *Langmuir* **2009**, 25, 9197-9207.
- 56 Faghihnejad, A. & Zeng, H. B. *Soft Matter* **2012**, 8, 2746-2759.
- 57 Mahnke, J., Stearnes, J., Hayes, R. A., Fornasiero, D. & Ralston, J. *Physical Chemistry Chemical Physics* **1999**, 1, 2793-2798.
- 58 Zhang, X. H., Zhang, X. D., Lou, S. T., Zhang, Z. X., Sun, J. L. & Hu, J. *Langmuir* **2004**, 20, 3813-3815.
- 59 Ishida, N., Inoue, T., Miyahara, M. & Higashitani, K. *Langmuir* **2000**, 16, 6377-6380.
- 60 Ishida, N., Sakamoto, M., Miyahara, M. & Higashitani, K. *Journal of Colloid and Interface Science* **2002**, 253, 112-116.
- 61 Lou, S., Gao, J., Xiao, X., Li, X., Li, G., Zhang, Y., Li, M., Sun, J. & Hu, J. *Mat. Char.* **2002**, 48, 211-214.
- 62 Sakamoto, M., Kanda, Y., Miyahara, M. & Higashitani, K. *Langmuir* **2002**, 18, 5713-5719.
- 63 Simonsen, A. C., Hansen, P. L. & Klosgen, B. *Journal of Colloid and Interface Science* **2004**, 273, 291-299.
- 64 Zhang, X. H., Maeda, N. & Craig, V. S. J. *Langmuir* **2006**, 22, 5025-5035.
- 65 Yang, J., Duan, J., Fornasiero, D. & Ralston, J. *Journal of Physical Chemistry B* **2003**, 107, 6139-6147.
- 66 Zhang, X. H., Quinn, A. & Ducker, W. A. *Langmuir* **2008**, 24, 4756-4764.
- 67 Tyrrell, J. W. G. & Attard, P. *Physical Review Letters* **2001**, 87, 176104.



- 68 Tyrrell, J. & Attard, P. *Langmuir* **2002**, 18, 160-167.
- 69 McKee, C. T. & Ducker, W. A. *Langmuir* **2005**, 21, 12153-12159.
- 70 Steitz, R., Gutberlet, T., Hauss, T., Klosgen, B., Krastev, R., Schemmel, S., Simonsen, A. C. & Findenegg, G. H. *Langmuir* **2003**, 19, 2409-2418.
- 71 Thormann, E., Simonsen, A. C., Hansen, P. L. & Mouritsen, O. G. *ACS nano* **2008**, 2, 1817-1824.
- 72 Thomson, W. T. *Philosophical Magazine* **1871**, 42, 448.
- 73 Butt, H. J. & Kappl, M. *Advances in Colloid and Interface Science* **2009**, 146, 48-60.
- 74 Eriksson, J. C., Ljunggren, S. & Claesson, P. M. *Journal of the Chemical Society, Faraday Transactions 2* **1989**, 85, 163-176.
- 75 Eriksson, J. C. & Henriksson, U. *Langmuir* **2007**, 23, 10026-10033.
- 76 Vinogradova, O. I. *Langmuir* **1995**, 11, 2213-2220.
- 77 Ruckenstein, E. *Journal of colloid and interface science* **1997**, 188, 218-223.
- 78 Evans, D., Craig, V. & Senden, T. *Physica A: Statistical Mechanics and its Applications* **2004**, 339, 101-105.
- 79 Vinogradova, O. I., Yakubov, G. E. & Butt, H. J. *The Journal of Chemical Physics* **2001**, 114, 8124.
- 80 Rabinovich, Y. I. & Yoon, R. H. *Colloids and Surfaces A: Physicochemical and Engineering Aspects* **1994**, 93, 263-273.
- 81 Ishida, N. & Higashitani, K. *Minerals Engineering* **2006**, 19, 719-725.
- 82 Serro, A. P., Colaco, R. & Saramago, B. *Journal of Colloid and Interface Science* **2008**, 325, 573-579.
- 83 Jung, Y. C. & Bhushan, B. *Nanotechnology* **2006**, 17, 4970.
- 84 Dupré, A. & Dupré, P. *Théorie mécanique de la chaleur*. (Gauthier-Villars, 1869).
- 85 Johnson, K., Kendall, K. & Roberts, A. *Proceedings of the Royal Society of London. A. Mathematical and Physical Sciences* **1971**, 324, 301-313.
- 86 Amontons, G. *Mémoires de l'Académie Royale des Sciences Paris* **1699**.
- 87 Coulomb, C. A. *Mémoires de Mathématique et de Physique Paris* **1785**, 161-342.
- 88 Ruan, J. A. & Bhushan, B. *Journal of Applied Physics* **1994**, 76, 5022-5035.
- 89 Berman, A., Drummond, C. & Israelachvili, J. *Tribology letters* **1998**, 4, 95-101.
- 90 Gao, J., Luedtke, W., Gourdon, D., Ruths, M., Israelachvili, J. N. & Landman, U. *The Journal of Physical Chemistry B* **2004**, 108, 3410-3425.

- 91 Bowden, F. & Tabor, D. *Proceedings of the Royal Society of London. Series A, Mathematical and Physical Sciences* **1939**, 169, 391-413.
- 92 Kusy, R. & Whitley, J. Q. *Journal of Biomechanics* **1990**, 23, 913-925.
- 93 Menezes, P. L. & Kailas, S. V. *Journal of Tribology* **2006**, 128, 697.
- 94 Thormann, E., Yun, S. H., Claesson, P. M. & Linnros, J. *ACS Applied Materials & Interfaces* **2011**.
- 95 Pilkington, G. A., Thormann, E., Claesson, P. M., Fuge, G. M., Fox, O. J. L., Ashfold, M. N. R., Leese, H., Mattia, D. & Briscoe, W. H. *Physical Chemistry Chemical Physics* **2011**, 13, 9318-9326.
- 96 Koinkar, V. N. & Bhushan, B. *Journal of applied physics* **1997**, 81, 2472.
- 97 Stiernstedt, J., Nordgren, N., Wågberg, L., Brumer, H., Gray, D. G. & Rutland, M. W. *Journal of Colloid and Interface Science* **2006**, 303, 117-123.
- 98 Homola, A. M., Israelachvili, J. N., McGuiggan, P. M. & Gee, M. L. *Wear* **1990**, 136, 65-83.
- 99 Israelachvili, J. N., Chen, Y. L. & Yoshizawa, H. *Journal of Adhesion Science and Technology* **1994**, 8, 1231-1249.
- 100 Feiler, A. A., Jenkins, P. & Rutland, M. W. *Journal of Adhesion Science and Technology*, 19 **2005**, 3, 165-179.
- 101 Feiler, A. A., Stiernstedt, J., Theander, K., Jenkins, P. & Rutland, M. W. *Langmuir* **2007**, 23, 517-522.
- 102 Young, T. *Philosophical Transactions of the Royal Society of London* **1805**, 95, 65-87.
- 103 Wenzel, R. N. *Industrial & Engineering Chemistry* **1936**, 28, 988-994.
- 104 Cassie, A. B. D., Baxter, S. *Transactions of the Faraday Society* **1944**, 40, 546-551.
- 105 Patankar, N. A. *Langmuir* **2004**, 20, 7097-7102.
- 106 Tuberquia, J. C., Song, W. S. & Jennings, G. K. *Analytical Chemistry* **2011**.
- 107 Bico, J., Marzolin, C. & Quéré, D. *Europhysics Letters* **1999**, 47, 220.
- 108 Gao, L. & McCarthy, T. J. *Langmuir* **2007**, 23, 3762-3765.
- 109 Pease, D. C. *The Journal of Physical Chemistry* **1945**, 49, 107-110.
- 110 Bartell, F. & Shepard, J. *The Journal of Physical Chemistry* **1953**, 57, 455-458.
- 111 Chen, W., Fadeev, A. Y., Hsieh, M. C., Öner, D., Youngblood, J. & McCarthy, T. J. *Langmuir* **1999**, 15, 3395-3399.
- 112 Öner, D. & McCarthy, T. J. *Langmuir* **2000**, 16, 7777-7782.

- 113 Extrand, C. *Langmuir* **2003**, 19, 3793-3796.
- 114 Yamamoto, K. & Ogata, S. *Journal of Colloid and Interface Science* **2008**, 326, 471-477.
- 115 Erbil, H. Y. & Cansoy, C. E. *Langmuir* **2009**, 25, 14135-14145.
- 116 Panchagnula, M. V. & Vedantam, S. *Langmuir* **2007**, 23, 13242.
- 117 McHale, G. *Langmuir* **2007**, 23, 8200-8205.
- 118 Nosonovsky, M. *Langmuir* **2007**, 23, 9919-9920.
- 119 Milne, A. & Amirfazli, A. *Advances in Colloid and Interface Science* **2012**, 170, 48-55.
- 120 Binnig, G., Quate, C. F. & Gerber, C. *Physical Review Letters* **1986**, 56, 930-933.
- 121 Ducker, W. A., Senden, T. J. & Pashley, R. M. *Nature* **1991**, 353, 239-241.
- 122 Ducker, W. A., Senden, T. J. & Pashley, R. M. *Langmuir* **1992**, 8, 1831-1836.
- 123 Sader, J. E., Chon, J. W. M. & Mulvaney, P. *Review of Scientific Instruments* **1999**, 70, 3967-3969.
- 124 Hutter, J. L. & Bechhoefer, J. *Review of Scientific Instruments* **1993**, 64, 1868-1873.
- 125 Cleveland, J., Manne, S., Bocek, D. & Hansma, P. *Review of Scientific Instruments* **1993**, 64, 403-405.
- 126 Preuss, M. & Butt, H. *Journal of Colloid and Interface Science* **1998**, 208, 468-477.
- 127 Preuss, M. & Butt, H. J. *Langmuir* **1998**, 14, 3164-3174.
- 128 Johnson, D. J., Miles, N. J. & Hilal, N. *Advances in Colloid and Interface Science* **2006**, 127, 67-81.
- 129 Maeda, Y., Yamamoto, H. & Ikeda, I. *Macromolecules* **2003**, 36, 5055-5057.
- 130 Maeda, Y., Yamamoto, H. & Ikeda, I. *Langmuir* **2004**, 20, 7339-7341.
- 131 He, P., Bitla, S., Bousfield, D. & Tripp, C. P. *Applied Spectroscopy* **2002**, 56, 1115-1121.
- 132 Vyorykka, J., Vuorinen, T. & Bousfield, D. W. *Nordic Pulp & Paper Research Journal* **2004**, 19, 218-223.
- 133 Clarke, F. C., Jamieson, M. J., Clark, D. A., Hammond, S. V., Jee, R. D., Moffat, A. C. *Analytical Chemistry* **2001**, 73, 2213-2220.
- 134 Dieing, T., Holtricher, O. & Toporski, J. *Confocal Raman Microscopy*. Vol. 158 (Springer Verlag, 2011).
- 135 Raman, C. *Indian Journal of physics* **1928**, 2, 387-398.
- 136 Schmitt, M. & Popp, J. *Journal of Raman Spectroscopy* **2006**, 37, 20-28.
- 137 Tabaksblat, R., Meier, R.J., Kip, B.J. *Applied Spectroscopy* **1992**, 46, 60.

- 138 Turell, G., Dhamelincourt, P. *Micro-Raman spectroscopy* (John Wiley & Sons, 1996).
- 139 Wilson, T. *Optical aspects of confocal Microscopy* (Academic press, London, 1990).
- 140 Vyörykkä, J., Haltunen, M., Iitti, H., Tenhunen, J., Vuorinen, T., Stenius, P. *Applied Spectroscopy* **2002**, 56, 2.
- 141 Griffith, P. & Haseth, J. *Fourier transform infrared spectroscopy*. (John Wiley&Sons, New York, 1986).
- 142 Ulman, A. *An introduction to Ultrathin Organic Films from Langmuir-Blodgett to Self-Assembly*. (Academic Press: San Diego, 1991).
- 143 Zasadzinski, J. A., Viswanathan, R., Madsen, L., Garnaes, J. & Schwartz, D. K. *Science* **1994**, 263, 1726-1733.
- 144 Ulman, A. *Advanced Materials* **1990**, 2, 573-582.
- 145 Kurthen, C. & Nitsch, W. *Thin Solid Films* **1990**, 188, L5-L8.
- 146 Xu, J. & Li, H. L. *Journal of Colloid and Interface Science* **1995**, 176, 138-149.
- 147 Tredgold, R. H. *Journal of Materials Chemistry* **1995**, 5, 1095-1106.
- 148 Chang, C., Wang, Y. F., Kanamori, Y., Shih, J. J., Kawai, Y., Lee, C. K., Wu, K. C. & Esashi, M. *Journal of Micromechanics and Microengineering* **2005**, 15, 580.
- 149 Nagayama, K. *Colloids and Surfaces A-Physicochemical and Engineering Aspects* **1996**, 109, 363-374.
- 150 Kralchevsky, P. A. & Denkov, N. D. *Current Opinion in Colloid & Interface Science* **2001**, 6, 383-401.
- 151 Yasuda, H., Yasuda, H. K., Chemiker, J. & Chemist, J. *Plasma polymerization*. (Academic Press New York, 1985).
- 152 Baralia, G. G., Pallandre, A., Nysten, B. & Jonas, A. M. *Nanotechnology* **2006**, 17, 1160.
- 153 Tsai, P. S., Yang, Y. M. & Lee, Y. L. *Langmuir* **2006**, 22, 5660-5665.
- 154 Lee, Y. L., Du, Z. C., Lin, W. X. & Yang, Y. M. *Journal of Colloid and Interface Science* **2006**, 296, 233-241.
- 155 Wählander, M. *Development and Characterization of Superhydrophobic Surfaces – AFM Colloidal Probe Measurements between Superhydrophobic, Hydrophobic and Hydrophilic Surfaces in Liquid Cell* M.Sc. thesis, Royal Institute of Technology, KTH, (2008).
- 156 Oudrhiri-Hassani, F., Presmanes, L., Barnabé, A. & Tailhades, P. *Applied Surface Science* **2008**, 254, 5796-5802.
- 157 Nakae, H., Inui, R., Hirata, Y. & Saito, H. *Acta Materialia* **1998**, 46, 2313-2318.
- 158 Marmur, A. & Bittoun, E. *Langmuir* **2009**, 25, 1277-1281.

- 159 Evans, D. F. & Wennerström, H. *The colloidal domain*. (Wiley-  
VCH: New York, 1999).
- 160 Singh, S., Houston, J., van Swol, F. & Brinker, C. J. *Nature*  
**2006**, 442, 526-526.
- 161 Du, Q., Freysz, E. & Shen, Y. R. *Science* **1994**, 264, 826-828.
- 162 Ye, S., Nihonyanagi, S. & Uosaki, K. *Physical Chemistry*  
*Chemical Physics* **2001**, 3, 3463-3469.
- 163 Liu, W. T., Zhang, L. N. & Shen, Y. R. *Journal Of Chemical*  
*Physics* **2006**, 125.
- 164 Ljunggren, S. & Eriksson, J. C. *Colloids and Surfaces A-*  
*Physicochemical and Engineering Aspects* **1997**, 130, 151-155.
- 165 Wennerström, H. *Journal of Physical Chemistry B* **2003**, 107,  
13772-13773.
- 166 He, Y., Jiang, C. Y., Yin, H. X., Chen, J. & Yuan, W. Z. *Journal*  
*of Colloid and Interface Science* **2011**, 364, 219-229.